LAVA Simulations for the AIAA Sonic Boom Prediction Workshop

Jeffrey A. Housman[*1], Emre Sozer[*2],
Shayan Moini-Yekta[*2], and Cetin C. Kiris[†1]

[1]*NASA Ames Research Center, Moffett Field, CA 94035*
[2]*Science and Technology Corporation, Moffett Field, CA 94035*

Computational simulations using the Launch Ascent and Vehicle Aerodynamics (LAVA) framework are presented for the First AIAA Sonic Boom Prediction Workshop test cases. The framework is utilized with both structured overset and unstructured meshing approaches. The three workshop test cases include an axisymmetric body, a Delta Wing-Body model, and a complete low-boom supersonic transport concept. Solution sensitivity to mesh type and sizing, and several numerical convective flux discretization choices are presented and discussed. Favorable comparison between the computational simulations and experimental data of near- and mid-field pressure signatures were obtained.

Nomenclature

M_∞	Free-stream Mach number
α	Angle of attack
h	Distance between model and solution extraction line
Φ	Angle between model centerline and solution extraction line
Re	Reynolds number per meter
$\Delta p/p_\infty$	Pressure $(p - p_\infty)$ divided by p_∞
ALR	Aft-Lift Relaxation
RANS	Reynolds Averaged Navier-Stokes
CFD	Computational Fluid Dynamics
LAVA	Launch Ascent and Vehicle Aerodynamics

I. Introduction

One of the main barriers to commercially viable civilian supersonic transports is the noise generated due to sonic boom. In order to reduce the ground level noise, aerodynamic shape optimization can be used to minimize the sonic boom, and has become an active research area.[1–3] Computational Fluid Dynamics (CFD) plays a critical role in understanding the mechanisms responsible for sonic boom generation and can be used to assist in the boom minimization process. Validation of CFD

---

[*]Research Scientist, Applied Modeling and Simulation Branch, NAS Division, MS N258-2, AIAA Senior Member
[†]Branch Chief, Applied Modeling and Simulation Branch, NAS Division, MS N258-2, AIAA Senior Memeber

American Institute of Aeronautics and Astronautics

prediction capabilities for sonic boom applications is required to provide confidence in the accuracy of the numerical methods. The First AIAA Sonic Boom Prediction Workshop,[4] is a step towards validation of CFD prediction capabilities on sonic boom problems. Three test cases of varying geometric complexity were analyzed in the workshop; an axisymmetric body, a Delta Wing-Body (DWB) model, and a complete low-boom supersonic transport aircraft concept. LAVA results for the first two cases, mandatory for participation, were submitted to the workshop. The optional test case was recently completed and results are included herein.

A variety of computational methods and griding strategies have been applied to the sonic boom prediction workshop problems. A subset of these include, unstructured methods such as those employed by Park *et al.* [5] and Saito *et al.* [6] Both unstructured and overset structured grid methods were applied by Cliff *et al.*,[7] and an embedded-boundary Cartesian mesh method with adjoint-based error estimation was utilized by Aftosmis *et al.*[8] The goal of the current work is to validate the Launch Ascent and Vehicle Aerodynamics (LAVA) CFD solver modules [9] for sonic boom related applications. The CFD codes within LAVA were developed at NASA Ames Research Center to enable the use of a variety of meshing strategies, namely block structured Cartesian immersed-boundary, structured overset curvilinear, and unstructured. In this particular work, the structured overset and unstructured meshing strategies are assessed for the workshop test cases. For accurate structured overset meshing, approaches similar to those described in Meredith *et al.*[10] and Haering *et al.*[11] are used. Several unstructured grid approaches have been explored, and the work of Cliff *et al.*[12,13] provides the basis for this study.

The computational results for each workshop test case are presented along with detailed descriptions of the computational grids, numerical methods, and computing requirements. Comparison of computed results to available experimental data, and sensitivity analysis are discussed for each of the three test cases. A summary of the comparisons and recommendations for mesh generation to achieve accurate sonic boom prediction using LAVA are summarized in the final section.

II.   Numerical Methods

The LAVA CFD framework[9] offers highly flexible meshing options and was developed for robustly handling complex geometries. It supports block-structured Cartesian grids with Adaptive Mesh Refinement (AMR) and immersed-boundary capabilities, structured curvilinear overlapping grid systems, and unstructured arbitrary polyhedral meshes. In addition, overset coupling between Cartesian and unstructured meshes is available. The compressible Navier-Stokes equations are solved using second-order accurate finite-volume and/or finite-difference formulations. The Spalart-Allmaras (SA)[14] and Shear Stress Transport (SST)[15] turbulence models, as well as their Detached Eddy Simulation (DES) variants,[16,17] are implemented for turbulent flow simulations. Spatial discretization includes options for several flux difference and flux vector splitting schemes, such as the modified Roe with local preconditioning,[18,19] standard central with explicit scalar artificial dissipation,[20] and AUSMPW+.[21] A full description of the LAVA framework is given in Kiris *et al.*[9] A summary of the methods used for the sonic boom analysis presented in this work include:

Meshing	Convective Flux Discretization	Turbulence Model	Linear Solvers
Structured Overset	Modified Roe & Central	Spalart-Allmaras	Alternating line-Jacobi
Unstructured Polyhedral	AUSMPW+	Spalart-Allmaras	GMRES

American Institute of Aeronautics and Astronautics

III.   Computed Results

III.A.   Case 1: Seeb-ALR

The first test case of the AIAA Sonic Boom Prediction Workshop is to simulate Mach 1.6 flow around the Seeb-ALR (Aft Lift Relaxation) body of revolution model[3] at zero degrees angle of attack. A CAD representation of the "as-built" geometry was distributed by the workshop organizers to the participants, and is shown in Figure 1a along with line contours of pressure, $\Delta p/p_\infty = (pressure - p_\infty)/p_\infty$, in Figure 1b. The model consists of an axisymmetric body with a low-boom and low drag shape based on the work of Darden, George, and Seabass.[22,23] The Seeb body is modified for more realizable models of equivalent areas by a small increase in the diameter of the model, just downstream of the shoulder, before tapering down to the diameter of the sting. A close-up of the ALR region is shown in Figure 1c scaled $10:1$ in the radial direction. A schematic of the coordinate system used for extracting pressure signatures for comparison with experimental data is displayed in Figure 1d. The length of the model is 17.667 inches. The length of the modeled geometry, including the sting, is 68.63 inches. A full description of the computational grid and requirements, comparison to experimental data, and sensitivity analysis is described.
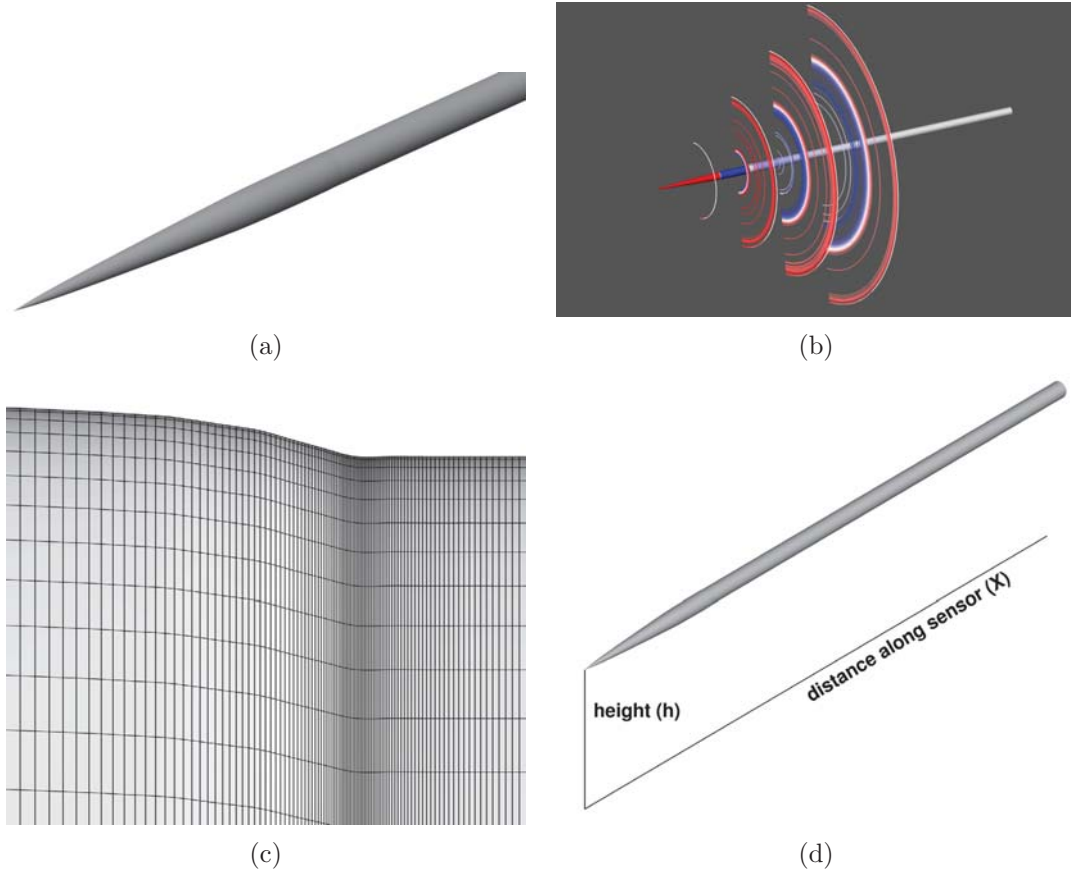

(a)

(b)

(c)

(d)

Figure 1. (a) Image of the Seeb-ALR "as-built" CAD model. (b) Line contours of dp/p_{inf} at several x-stations illustrating the axisymmetric flow-field. (c) Close-up of view of the Aft Lift Relaxation (ALR) region scaled $10:1$ in the radial direction. (d) Schematic of the coordinate system used to extract pressure for comparison with experimental results.

American Institute of Aeronautics and Astronautics

III.A.1. Computational Grid and Requirements

An overlapping grid system consisting of 4 structured grid zones and 21.7 million grid points was generated for the Seeb-ALR model. The grid system consists of a 3D axisymmetric conical grid split into two sections at the nose of the model. A cap grid at the nose is then generated to remove the singular axis from the body grid, and an additional shock capturing grid added just upstream of the blunt-nose to capture the bow shock. At the surface, the grid is normal to the body and generated with hyperbolic methods that smoothly transition to a highly stretched Mach-angle aligned grid. This improves accuracy of the boundary conditions at the wall and is required for viscous simulations to properly capture boundary layers in the wall normal direction.[24] Transitioning to a Mach-angle aligned grid is necessary to accurately and efficiently capture and propagate shock and expansion waves several body lengths away.[5, 25] Figure 2 shows three views of the overset grid system. A symmetry plane slice is shown to illustrate the Mach-angle aligned mesh as well as the clustering near the nose and shoulder regions of the model (left). The nose region, with a mesh aligned to the expected bow shock of the blunt nose, is shown on the top-right. The near wall transition region demonstrating the turning of the grid from the wall normal direction to the Mach-angle alignment is shown on the bottom-right.

Simulations were performed for the Seeb-ALR model using the LAVA CFD solver on the *Pleiades* supercomputer as NASA Ames Research Center. Converged solutions on the overset grid system were obtained in less than 1000 iterations using an alternating line Jacobi relaxation procedure on 4 Westmere nodes with 12 cores on each node for a total of 48 CPUs. Inviscid simulations required 1 hour and 30 minutes using modified Roe flux difference splitting with second-order MUSCL reconstruction and 1 hour and 18 minutes using second-order central differencing with explicit $2^{nd}/4^{th}$ difference scalar dissipation. Viscous RANS simulations were also performed for this model and required 1 hour and 45 minutes and 1 hour and 30 minutes using the same number of cores, respectively. A single slice of the axisymmetric portion of the structured grid was extracted and used to perform unstructured computations with the AUSMPW+ flux. An example of the residual convergence history of the continuity equation (red) and the change in pressure (blue) is plotted in
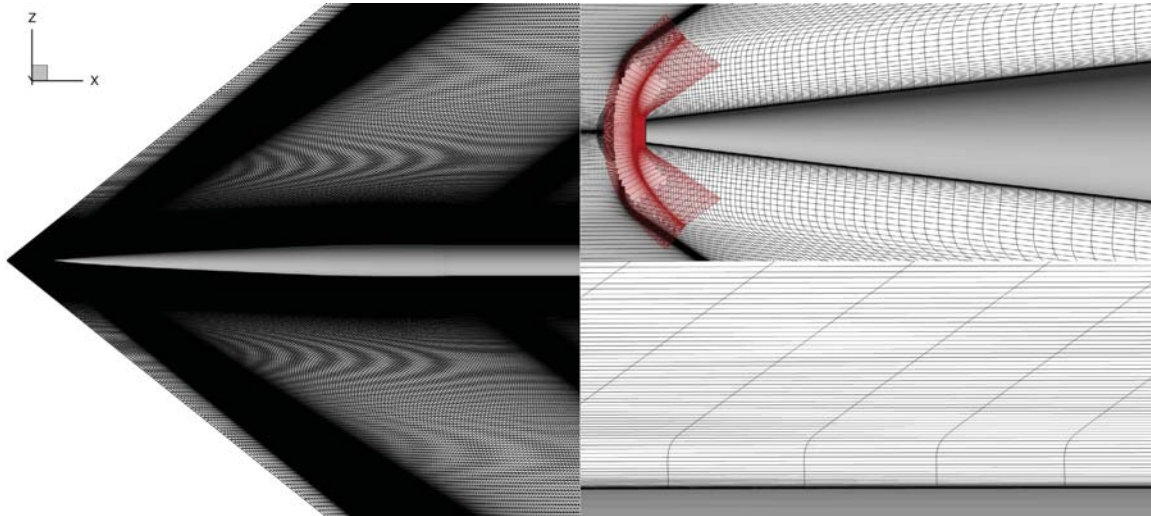

Figure 2. (left) Symmetry plane slice of the structured overset grid for the Seeb-ALR model illustrating the Mach-angle aligned mesh as well as clustering near the nose and ALR regions. (top-right) Close-up view of the nose region showing the bow-shock capturing grid (red) inserted upstream of the blunt nose. (bottom-right) Close-up view near the wall demonstrating the hyperbolic marching normal to the wall and the transition to the Mach-angle aligned mesh.
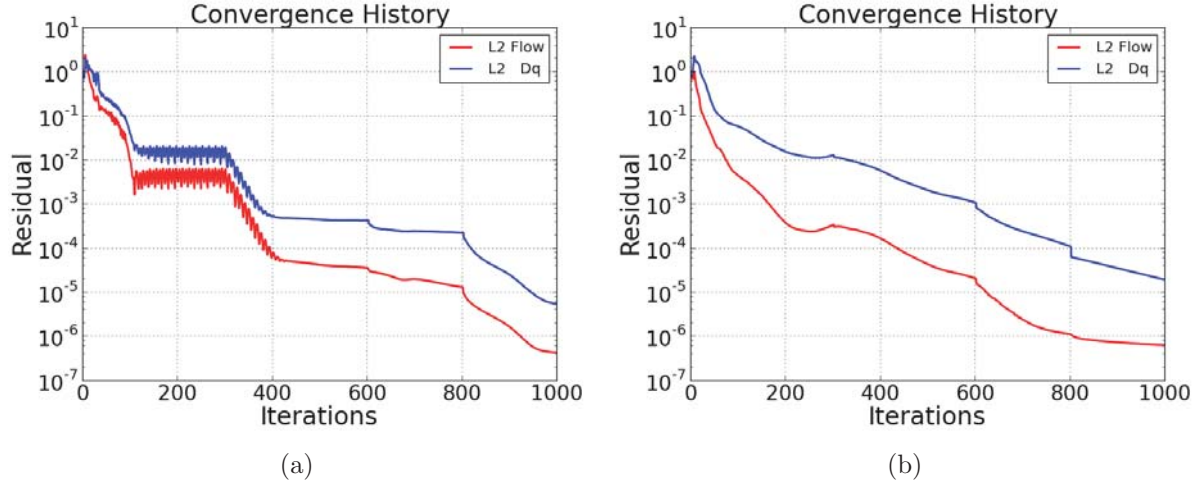
American Institute of Aeronautics and Astronautics

Figure 3. Residual convergence history for the Seeb-ALR test-case using (a) modified Roe flux difference splitting for the convective flux discretization and (b) central differencing with explicit scalar artificial dissipation.

Figure 3a and b. Slope discontinuities are observed in the convergence history at 300, 600, and 800 iterations which are associated with a manually prescribed CFL-ramping procedure to accelerate convergence as the solution evolves. The residual converges very rapidly after 300 iterations using the Roe scheme, then stalls until further ramping is applied. The central scheme results in a more monotonic decrease of the residual. This is likely caused by the non-smooth behavior of the *minmod* limiter used in the MUSCL reconstruction for the Roe scheme, compared to the smoother pressure switch used in the explicit artificial dissipation scheme.

III.A.2.   Data Comparison

Pressure signatures were extracted from the CFD solutions at two radial distances from the model, $h = 21.2$ inches and $h = 42.0$ inches, as requested in the workshop problem description. A third profile was extracted at $h = 31.2$ inches for comparison with the experimental data presented by Cliff *et al.*[7] Figure 4a shows a comparison of the CFD predicted pressure profile versus experimental measurements at $h = 21.2$ inches from the model. The different convective flux discretization options in LAVA lead to similar predicted signatures and reasonable agreement with the experimental data over the forward portion of the signal. Zooming into the bow shock portion, Figure 4b shows a slight under-shoot and over-shoot of the primary shock using central differencing, while the AUSMPW+ flux vector splitting appears to generate a small discontinuity possibly due to a *sonic glitch* in the numerical flux when the mesh is perfectly aligned, i.e. when the contravariant Mach number is unity. The Roe flux appears monotone and well behaved, but produces a much lower secondary peak than the central and AUSMPW+ schemes. A much sharper primary shock is predicted by the CFD solution than observed in the experimental data. This is likely caused by free-stream turbulence in the wind-tunnel, vibrations of the model, and averaging of pressure signatures, as discussed in Cliff *et al.*[7] Figure 4c shows a close-up view of the aft portion of the pressure signature where a larger discrepancy is observed between the CFD predictions and the experimental data. In order to determine which part of the model is generating the difference, a waterfall plot is used to trace the signature back to the model. Figure 4d shows a series of pressure profiles starting from just below the vehicle to the $h = 21.2$ inch location and plotted with the addition of a linear scaling function to separate the profiles. Tracing the expansion portion of the signal back to the geometry indicates

American Institute of Aeronautics and Astronautics

that the region near the shoulder modification portion of the geometry is where the difference occurs. Similar discrepancies have been observed by other workshop participants and several theories have been developed trying to explain the cause of the difference. Aftosmis and Nemec[8] re-measured the model to assess if any differences existed between the test article and the CAD model representation, finding only negligible differences. Theories based on pressure rail interaction,[26] wind-tunnel wall induced shock reflections, boundary layer effects, and model vibrations are currently being explored by the authors in collaboration with other participants from the workshop.
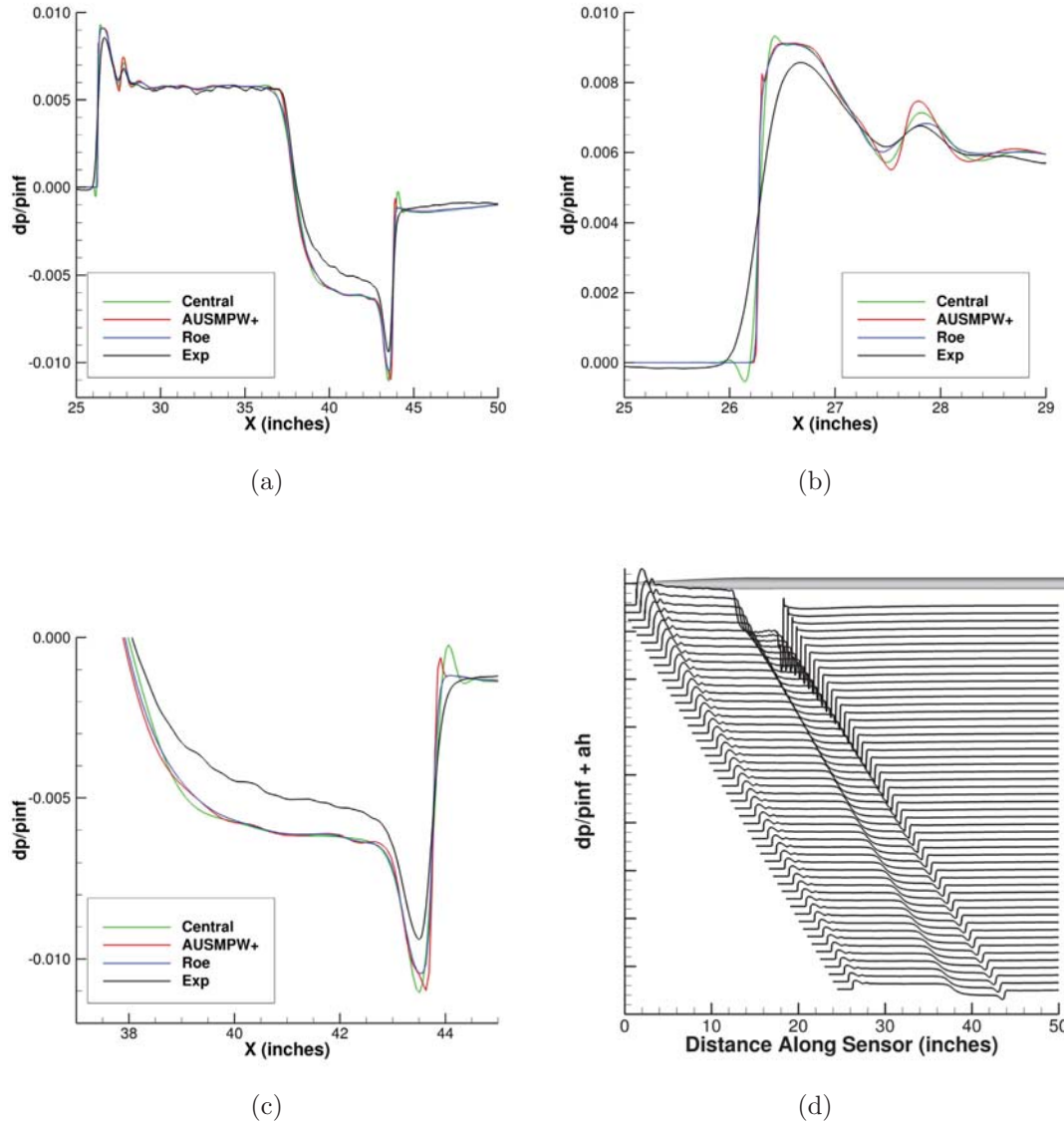
(a)

(b)

(c)

(d)

Figure 4. (a) Comparison of CFD predicted pressure versus experimental measurement at $h = 21.2$ inches from the model and $\phi = 0$ degrees for the Seeb-ALR model. (b) Close-up view of pressure signatures over first portion of the profile showing primary shock generated at the nose and the secondary shock caused by the diameter change in the body. (c) Close-up of aft portion of the signature showing a large discrepancy between the CFD predictions and the experimental data. (d) Waterfall plot of the pressure signatures starting from just below the model to $h = 21.2$ inches away.
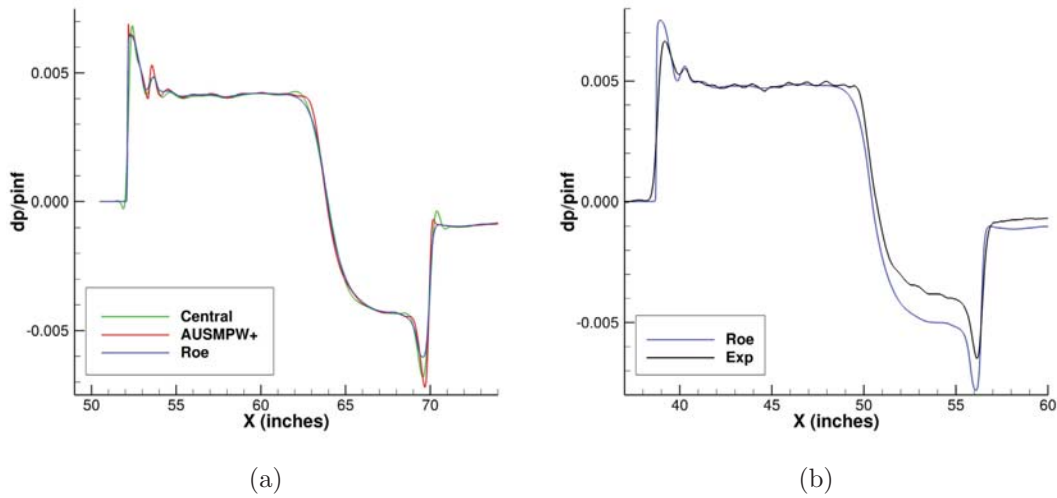
American Institute of Aeronautics and Astronautics

Figure 5. (a) Comparison of predicted pressure profiles at h = 42 inches and $\phi = 0$ degrees for the Seeb-ALR model using three convective flux discretization options in LAVA. (b) Comparison of pressure profiles at h = 31.2 inches and $\phi = 0$ degrees between experimental data and CFD prediction using the Roe flux.

An additional extraction at $h = 42.0$ inches, as requested by the workshop, is plotted in Figure 5a. Similar over- and under-shoots are observed using central differencing, but a pronounced pressure oscillation (relative to the other signatures) is observed using the AUSMPW+ flux. The strength of the small shock at $x = 53.5$ inches (just aft of the bow shock) is well matched between the central and Roe schemes, which are weaker than the AUSMPW+ flux results. The pressure level within the flat-top portion of the signatures are similar with all flux options applied, while the magnitude of the trailing shock is largest using AUSMPW+ and smallest using Roe. Experimental data at an additional extraction location of $h = 31.2$ inches was made available, and Figure 5b shows the data compared to the CFD prediction using the Roe convective flux. The comparison is nearly identical at this greater altitude to that shown in Figure 4a. A sharper primary shock and larger (in magnitude) expansion is predicted by the CFD compared to the experimental data.

III.A.3. Mesh and Turbulence Model Sensitivity

A series of mesh sensitivity studies were performed to assess the dependence of the predicted pressure signature on different characteristic parameters of the mesh. The first study assessed maximum axial spacing along the model geometry. Spacings from 0.02 to 0.2 inches were considered and no strong variations in the predicted pressure profiles were observed. Next, the axial spacing was fixed and sensitivity to the aspect ratio of the Mach-angle aligned portion of the mesh was studied. Figure 6a shows a diagram defining the aspect ratio related to the outer-most layer of the Mach-angle aligned mesh. Three meshes associated with aspect ratios of $AR = 10$, 20, and 40 were generated and inviscid Euler simulations were performed using the Roe scheme. Since a hyperbolic tangent stretching function was used from the grid transition region to the outer-most layer, each of the three aspect ratios lead to very modest stretching ratios far less than the 1.2 stretching used near the wall. Figure 6b shows the predicted pressure at $h = 42.0$ inches from the model for each of the three aspect ratios studied. Almost no difference is observed in the bow shock, while the level of the small shock at $x = 53.5$ inches appears to increase with decreasing aspect ratio. This is clearly shown in Figure 6c where the x-axis has been zoomed into the bow shock region. A similar increase in shock strength is observed for the tail shock in Figure 6d. It appears that the magnitude of the
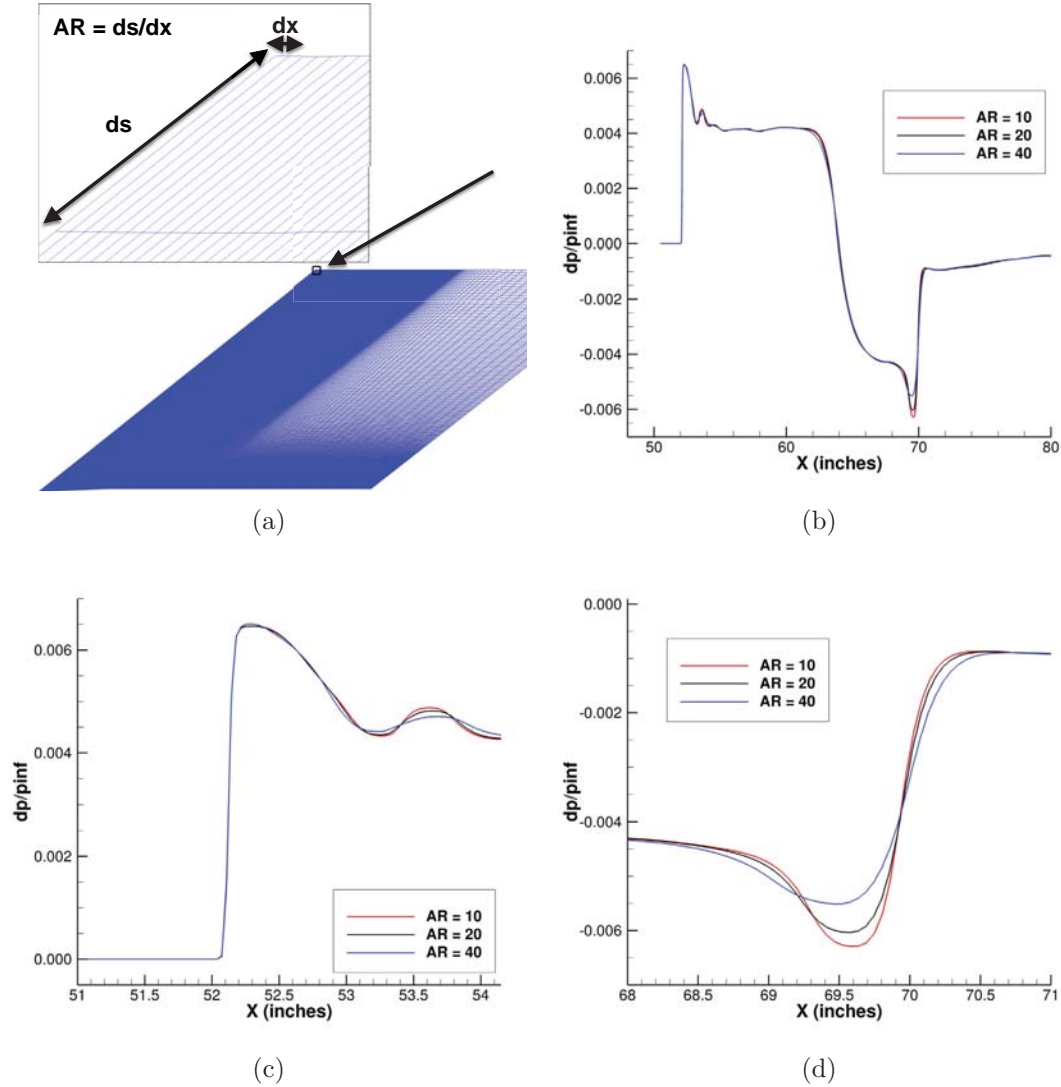
American Institute of Aeronautics and Astronautics

Figure 6. (a) Diagram illustrating the definition of aspect ratio AR = ds/dx used in the mesh sensitivity study for the Seeb-ALR model. (b) Comparison of pressure signatures at h = 42.0 inches from the Seeb-ALR model for three grid aspect ratios AR = 10, 20, and 40. (c) Close-up view of the pressure comparison over the primary and secondary shock locations. (d) Close-up view of the pressure comparison over the expansion and recovery regions.

change is reducing as the aspect ratio is decreased, indicating a trend toward mesh independence of the solution with respect to this particular mesh parameter. Solutions using the aspect ratio $AR = 20$ grid were submitted to the workshop and used for all the comparison plots in the previous section.

In order to assess the sensitivity of the predicted pressure signatures to the physical model equations, an additional Reynolds Averaged Navier-Stokes (RANS) solution was performed using the Spalart-Allmaras turbulence model.[14] Two near-wall mesh resolutions with $y+$ values of 1 and 2 were tested. No significant variation in the pressure signatures was observed between the two grids. Figure 7a shows the comparison between the RANS and Euler predictions with the experimental data at $h = 21.2$ inches. The modified Roe flux was used for both the Euler and the RANS results.
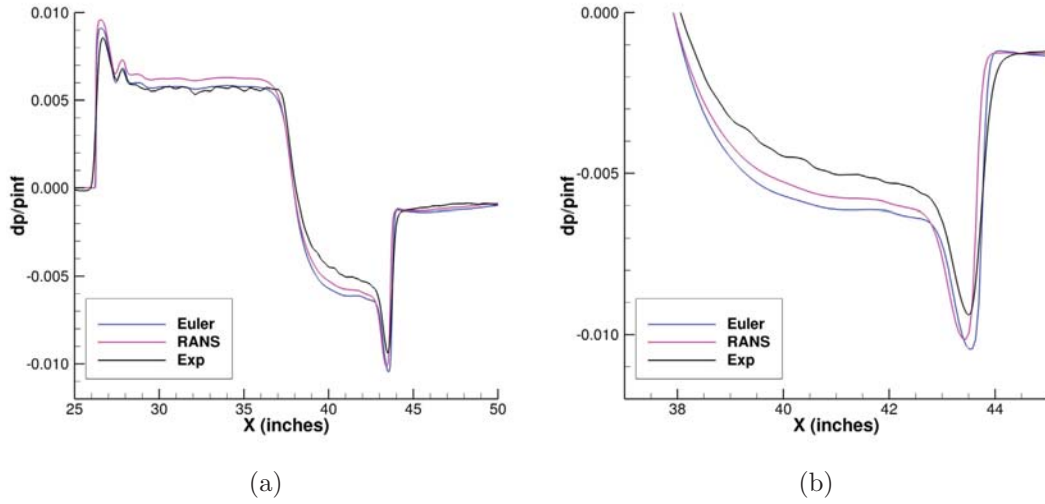
American Institute of Aeronautics and Astronautics

Figure 7. (a) Comparison of the pressure signatures using Euler and RANS models with experimental data at h = 21.2 inches from the Seeb-ALR model. (b) Close-up view of the pressure comparison over the expansion and recovery regions.

An almost constant offset is observed between the Euler and RANS predicted signatures over the forward shocks, the flat-top region, and the expansion/tail shock region. Note that the Reynolds number for the wind-tunnel was 4.36 million (per foot) for this case. It appears that the viscous boundary layer predicted by the RANS model is producing an effectively thicker body leading to a larger pressure in the primary and secondary shock regions as well as the flat-top region. One interesting feature is the decrease (in magnitude) of the pressure in the expansion region, as shown in Figure 7b. This offset is in the direction of the experimental data suggesting that boundary layer effects may have some contribution to the discrepancy between the CFD data and the experiment, and should be further explored in future investigations.

In summary, it appears that using the modified Roe flux difference splitting method for the convective flux and the Euler equations for the physical model provides the best comparison with the experimental data for the Seeb-ALR model. The central and AUSMPW+ flux options appear less dissipative than the Roe flux on the secondary shock, but contain numerical artifacts such as over- and under-shoots and small oscillations.

III.B. Case 2: 69° Delta-Wing-Body (DWB)

The second mandatory workshop test case is to simulate Mach 1.7 flow around a 69° Delta Wing Body (DWB), at zero degrees angle of attack. This case was solved using a RANS model for structured and unstructured grid approaches using a Reynolds number of 4.24 million (per foot) to match the wind-tunnel experiment. A CAD model of the geometry was provided by the workshop organizers. Details of the model along with early experimental work can be found in Hunton *et al.*[27] The model consist of a 69° swept delta wing bisecting a tangent ogive cylindrical fuselage, attached to an axisymmetric sting at the base of the model. The length of the model is 6.9 inches (30.4 inches including the sting provided in the CAD model) with a semi-span of 2.7 inches. Top, side, and perspective views of the DWB model are shown in Figure 8a - c, along with the coordinate system used for solution extraction and data comparison in Figure 8d. Note that since the model is not an axisymmetric model both on-track ($\phi = 0$ degrees) and off-track pressure signatures will be examined.

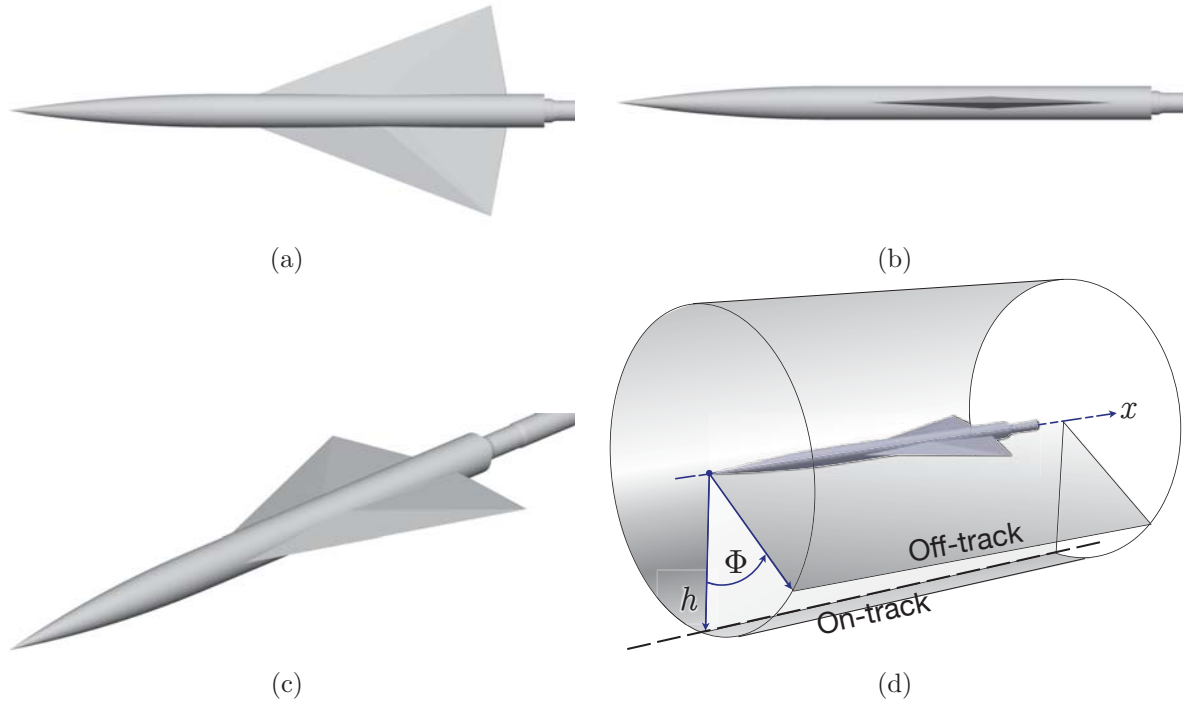American Institute of Aeronautics and Astronautics

Figure 8. (a) Top view of 69° Delta Wing Body (DWB) CAD model. (b) Side view of DWB model. (c) Perspective view of DWB model. (d) Coordinate system used for solution extraction and comparison to experimental data for DWB model.

III.B.1. Computational Grid and Requirements

Computational grids using both structured overset and unstructured grid techniques were generated for the 69° DWB model. The structured grid consists of 8 overlapping grid zones and 21.3 million grid points, while the unstructured mesh consists of 12.1 million polyhedral cells. In order to generate the structured overlapping grid system the fuselage-sting component of the DWB model is meshed first. A symmetry curve is generated along the axisymmetric fuselage/sting extending upstream and downstream along the singular axis. Hyperbolic marching from the symmetry curve in the wall normal direction is used throughout the boundary layer region. The mesh then transitions to a Mach-angle aligned grid and stretches to the outer-boundary using hyperbolic tangent stretching. Next, cap grids are generated to remove the axis singularities at the nose of the fuselage and end of the sting. Finally, the delta wing is meshed clustering at the leading and trailing edges of the wing as well as the wing-tip. Figure 9a-c displays the surface mesh for the overlapping grid system along with the grid-plane through the symmetry plane of the delta wing. Note how the wing component cuts the Mach-angle aligned mesh. Clustering on the fuselage body at the root of the leading and trailing edges of the delta wing help capture the leading and terminating shocks. Grid clustering is used upstream of the apex on the delta wing to ensure similar grid spacings at the wing-tip.

For the unstructured mesh, the surface of the DWB is tessellated with clustering near the nose, the base, and the sharp edges of the wing. A cylindrical surface is then generated which encompasses the entire DWB model and becomes the boundary for the polyhedral core grid (see Figure 10a). Once the polyhedral core grid is generated, prism layers are formed near the surface of the model and are transitioned into the core grid. Finally, the outer cylindrical surface of the core grid is extruded into a Mach-angle aligned grid using geometric stretching. Figure 10b illustrates the transition
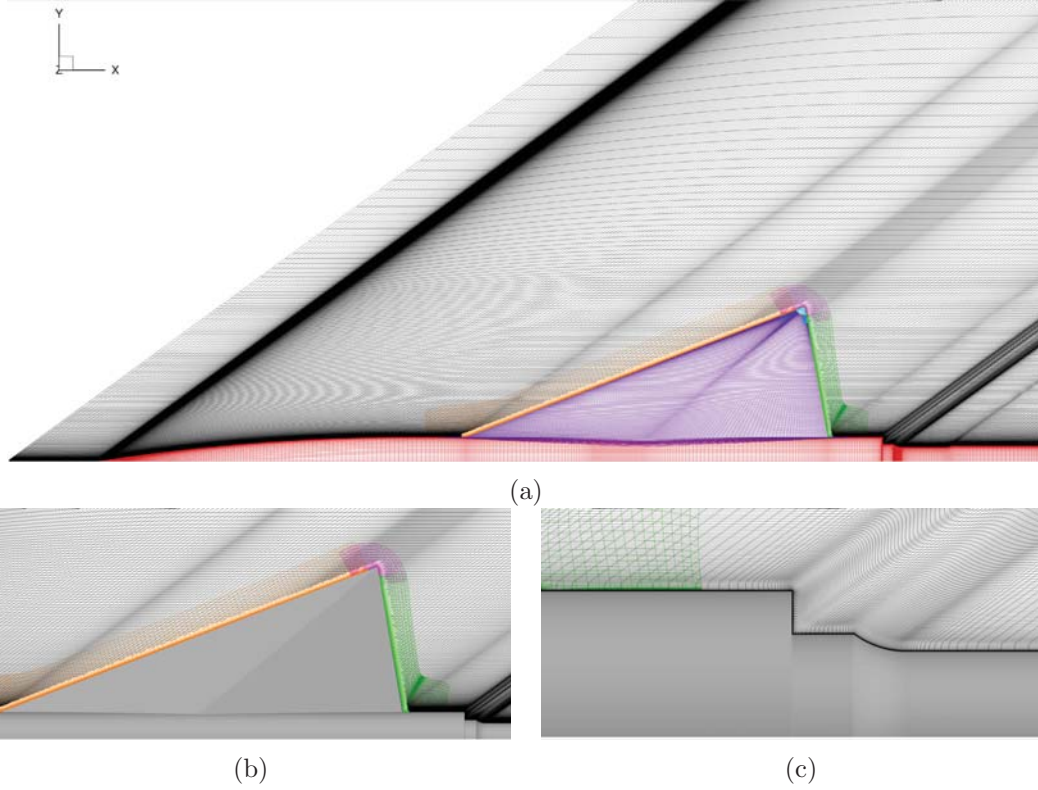
American Institute of Aeronautics and Astronautics

(a)

(b)

(c)

Figure 9. Body-fitted structured overlapping grid system for the $69°$ DWB configuration. (a) Close-up view of surface grid and a slice of the Mach-angle aligned grid. (b) Wing body junction highlighting overset hole-cutting of Mach-angle aligned grid by the delta wing. (c) Cone base region showing grid transition into the sting.
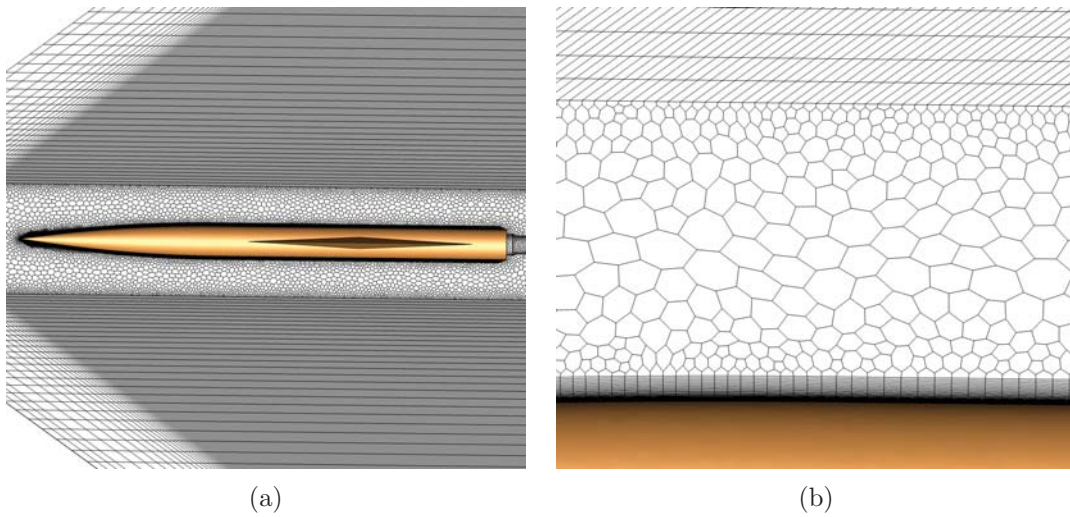

(a)

(b)

Figure 10. Unstructured polyhedral grid for the $69°$ DWB configuration. (a) Symmetry plane slice of the unstructured mesh showing the polyhedral core grid and the stretched Mach-angle aligned mid-field grid. (b) Close-up view of the prismatic boundary layer transitioning to a polyhedral core, then to a stretched Mach-angle aligned grid.
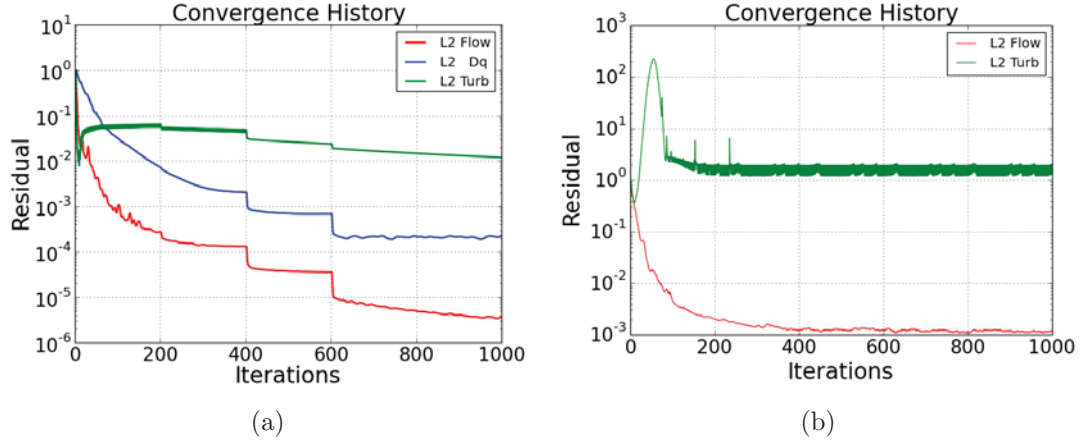
Figure 11. (a) Residual convergence history for the 69° DWB test-case using a structured overset grid system with modified Roe flux difference splitting. (b) Residual convergence history for the 69° DWB test-case using an unstructured polyhedral mesh with AUSMPW+ flux vector splitting.

between the near-wall prismatic layers, the core grid, and the stretched Mach-angle aligned grid.

Converged solutions for the DWB model were obtained on the overset grid system using 1000 iterations in 1 hour and 35 minutes and 1 hour and 49 minutes using 48 Westmere cores for the central differencing and modified Roe convective flux discretization options, respectively. The unstructured grid computations used 320 Sandy Bridge cores (approximately 1.8 times faster than a Westmere core) and converged in 25 minutes (1000 iterations) with the AUSMPW+ flux discretization. This is approximately a factor of 2 to 3 times more resources (total core-hours) using the unstructured mesh, but the grid generation is approximately a factor of 2-3 times less man hours for this configuration. In Figure 11 the residual convergence of the two different grid approaches is plotted. Effects of CFL-
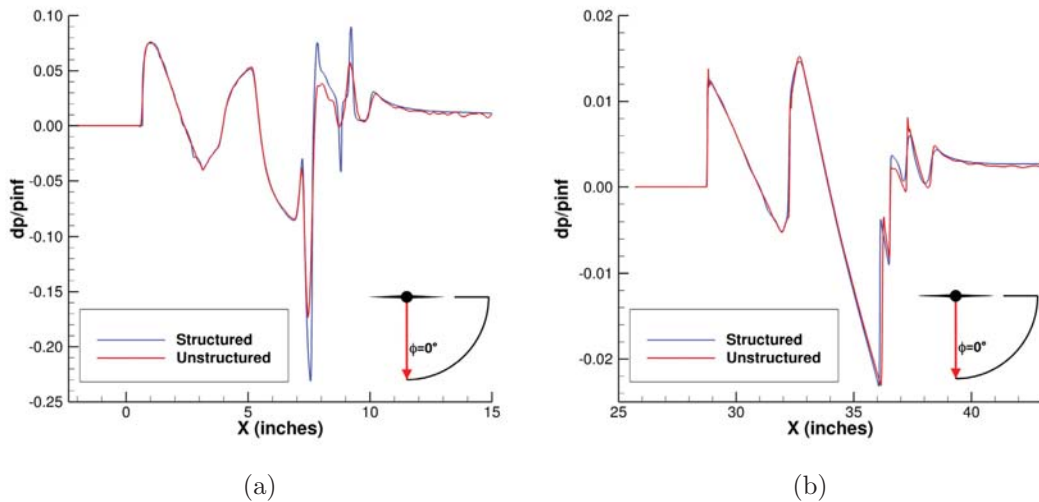

Figure 12. (a) Comparison of on-track near-field pressure signatures at h = 0.5 inches from the 69° DWB using structured overset and unstructured grids. (b) Comparison of on-track pressure signatures at h = 21.2 inches.

American Institute of Aeronautics and Astronautics

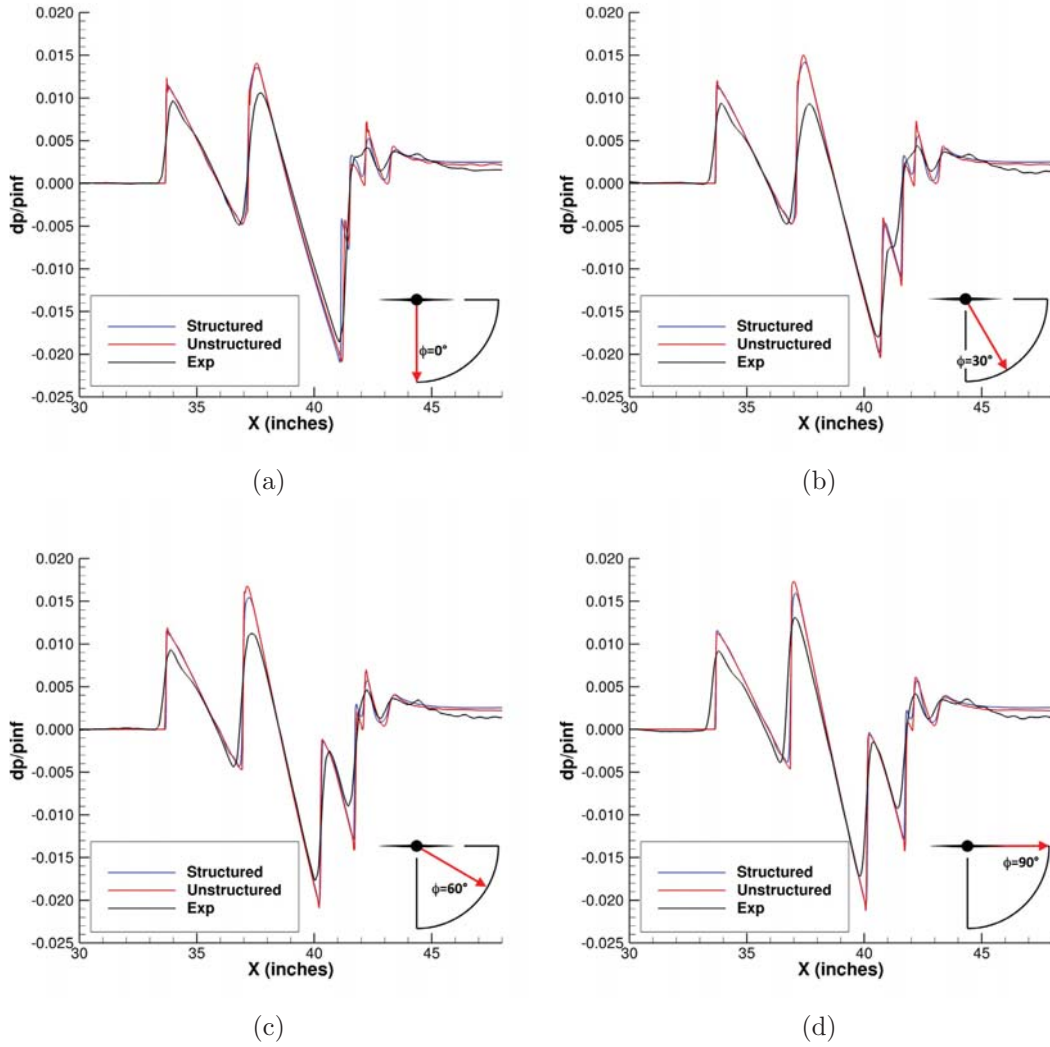**Figure 13. Predicted pressure signature comparison to experimental data for the 69° DWB at h = 24.8 inches using structured and unstructured grids: (a) $\phi = 0$ degrees, (b) $\phi = 30$ degrees, (c) $\phi = 60$ degrees, and (d) $\phi = 90$ degrees.**

ramping is indicated by the rapid reduction in residual values every 200 iterations. Good convergence of the field equations is obtained on both grid systems. The turbulence model convergence stalls after only a few orders. The source of the residual stalling appears to be downstream of the base on the sting, and maybe caused by small scale unsteadiness in the recirculation region. Running out to 5000 iterations did not improve the convergence. The pressures are well-converged in $200 - 400$ iterations.

III.B.2. Data Comparison

Ten line extraction locations were requested for the DWB test case; four on-track ($\phi = 0$ degrees) locations at $h = 0.5$, 21.2, 24.8, and 31.8 inches, and six off-track locations at $h = 24.8$ and 31.8 inches for $\phi = 30$, 60, and 90 degrees. Figure 12a compares the near-field on-track pressure signa-
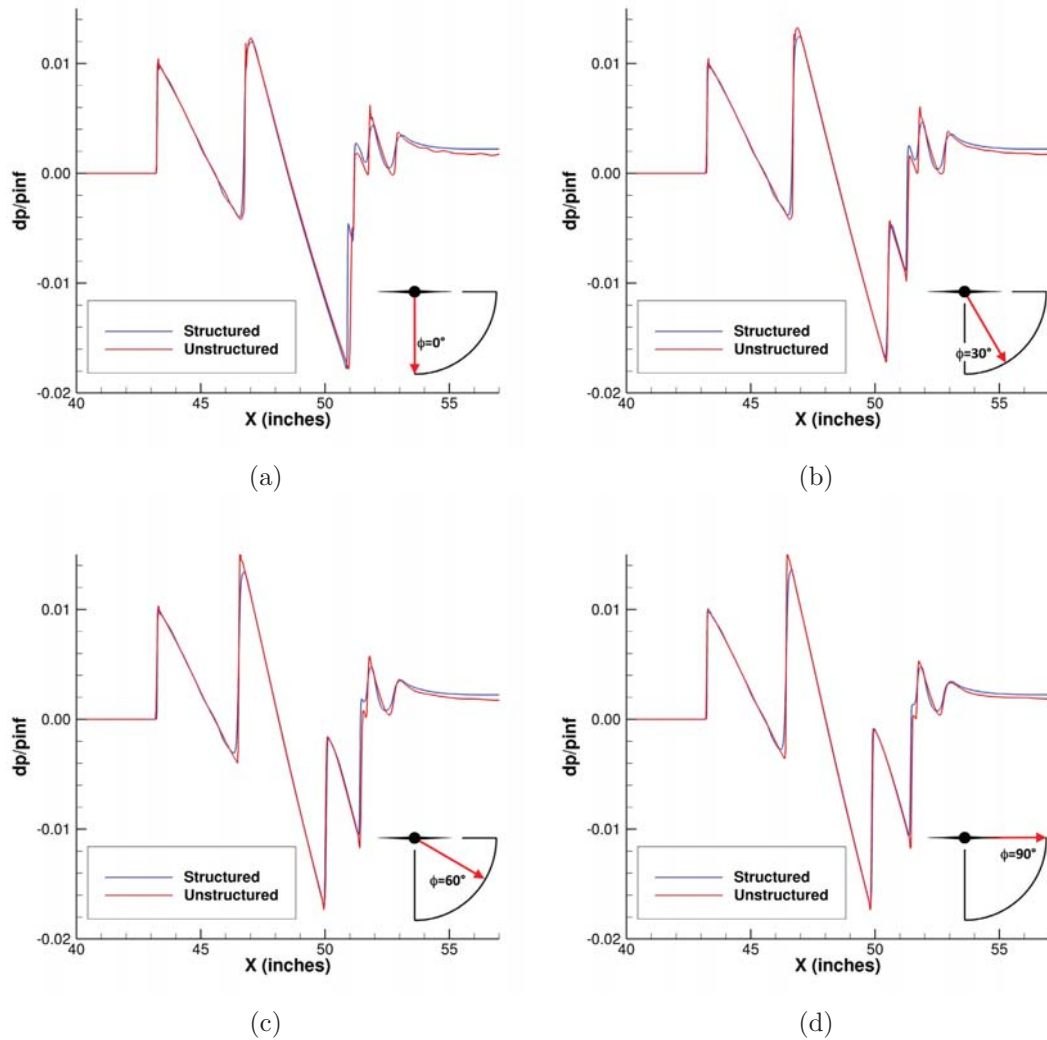
Figure 14. Far-field pressure signature comparison between structured and unstructured grids for the 69°
DWB at h = 31.8 inches: (a) $\phi = 0$ degrees, (b) $\phi = 30$ degrees, (c) $\phi = 60$ degrees, and (d) $\phi = 90$ degrees.

tures predicted using the structured overset grid with the modified Roe flux and the unstructured
polyhedral grid with the AUSMPW+ flux at $h = 0.5$ inches. The signatures match well over the first
portion of the signal associated with the forebody of the fuselage and front part of the delta wing.
Larger peak pressures are observed on the structured mesh over the aft portion of the signature, but
these differences decrease with attenuation as shown in Figure 12b at a distance of $h = 21.2$ inches.
At three body lengths, only small differences are observed in the location of the terminating shock
from the trailing edge of the delta wing, and minor shock strength differences in the base and sting
of the model. These differences in amplitude are likely caused by mesh resolution differences and a
lack of turbulence model convergence in the base region.

Experimental data obtained from Cliff *et al.*[7] at $h = 24.8$ inches is plotted against the CFD
predicted pressures for each ϕ angle in Figure 13a - d. The structured and unstructured grid results
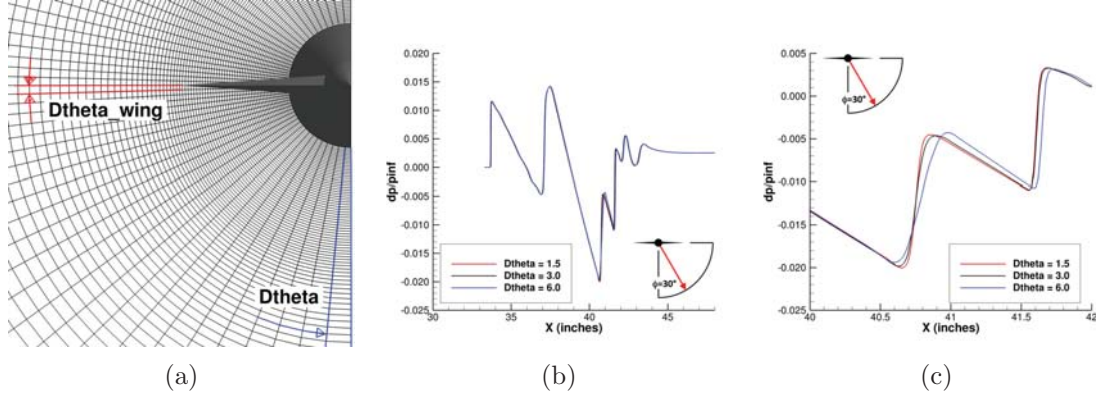agree well with each other and are relatively close to the experimental results. Position of the

American Institute of Aeronautics and Astronautics

Figure 15. (a) Diagram illustrating circumferential spacing variation from the symmetry plane to the wing tip. (b) Sensitivity comparison of pressure signatures for the 69° DWB model with respect to three different circumferential spacings Dtheta = 1.5, 3, and 6 degrees at h = 24.8 inches and ϕ = 30 degrees. (c) Close-up view pressure signature comparison over the terminating shock from the trailing edge of the delta wing.

shocks and slopes of the expansions associated with the fuselage agree with experiment, but the CFD peaks are considerably larger. The same is true for the shocks and expansions emanating from the delta wing, but at ϕ = 0 degrees the CFD predicts a shock at approximately 41.5 inches along the sensor which is not observed in the experimental measurement. This shock is associated with the terminating shock from the trailing edge of the delta wing and is visible in both the experiment and CFD results at off-track locations, although the strength of this shock is very weak in the experimental data at ϕ = 30 degrees. The propagated signal further from the model, at a distance of h = 31.8 inches is shown in Figure 14a - d for both on-track and off-track locations. At 4.6 body lengths, the structured and unstructured results are nearly identical to each other with only minor variations shock strengths.

III.B.3. Mesh Sensitivity

A series of three meshes were generated using different circumferential spacings. As shown in Figure 15a the circumferential spacing of the Mach-angle aligned grids start at the symmetry plane with a prescribed arc-length associated with an angle denoted *Dtheta* (in degrees). The arc-length is then reduced as the mesh revolves towards the wing in order to match the spacing of the volume grid near the wing tip, which is associate with an angle denoted as *Dtheta_wing*. Fixing *Dtheta_wing*, and using *Dtheta* = 1.5, 3, and 6 degrees, three overset grids were generates and the RANS solution was computed using the modified Roe flux discretization. Predicted pressure signatures for these simulations are plotted against each other in Figure 15b at h = 24.8 inches and ϕ = 30 degrees. The signatures are almost indistinguishable over most of the distance along the sensor. Sensitivity of the pressure signature to circumferential spacing is observed by zooming in on the terminating shock from the trailing edge of the delta wing, shown in Figure 15c. A small shift in shock position is observed when reducing *Dtheta* from 6 degrees to 3 degrees. Only a small variation is discernible when further reducing to 1.5 degrees. Results for the *Dtheta* = 3 degrees were reported to the workshop.

American Institute of Aeronautics and Astronautics

Figure 16. Three-view of the Lockheed Martin 1021 wind tunnel test article.

III.C.   Case 3: Lockheed Martin 1021 (LM1021)

A complete low-boom supersonic transport concept was included as an optional test case for the workshop. The Lockheed Martin Phase I low sonic boom model, designated the 1021 model, was designed to achieve low-boom on-track signatures and reduced off-track overpressures up to 20 degrees. The reference length of the LM 1021 is 22.365 inches and represents a 0.008 percent $(1 : 125)$ model of the flight-scale aircraft. A blade strut is used to hold the model in place and is swept greater than the Mach angle to minimize interference with the measured pressure signatures. Figure 16 shows a three-view of the configuration, note that one of the nacelles is located behind the blade strut between the v-shaped tail. Since the strut is located upstream of the flow-through nacelle,

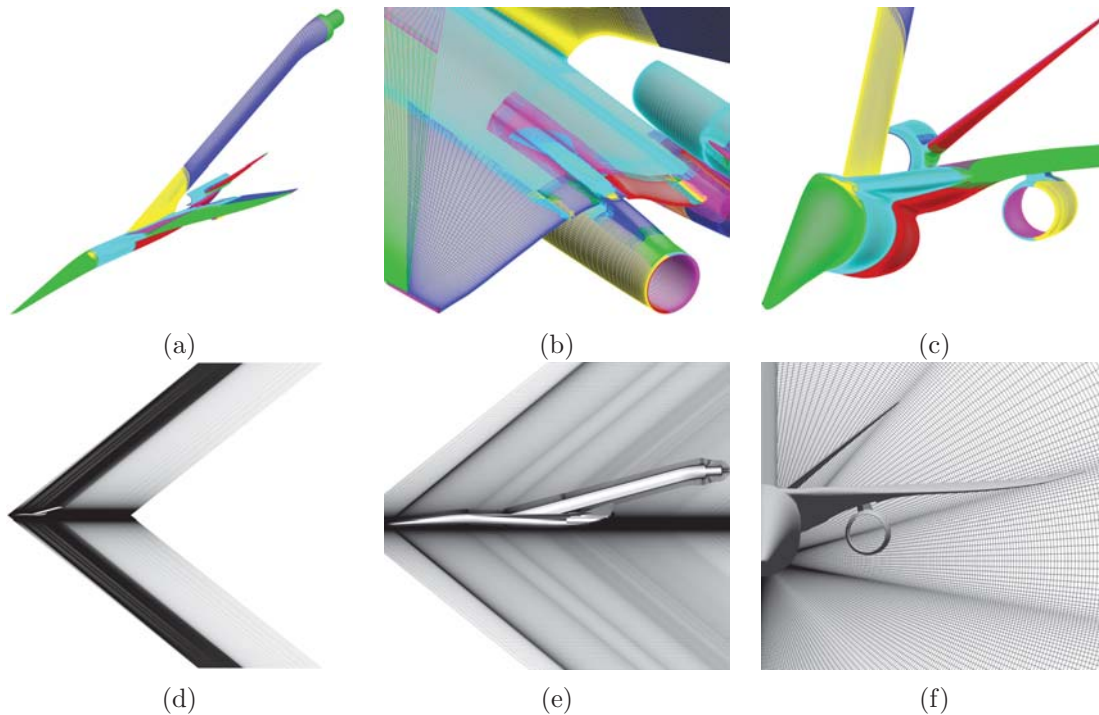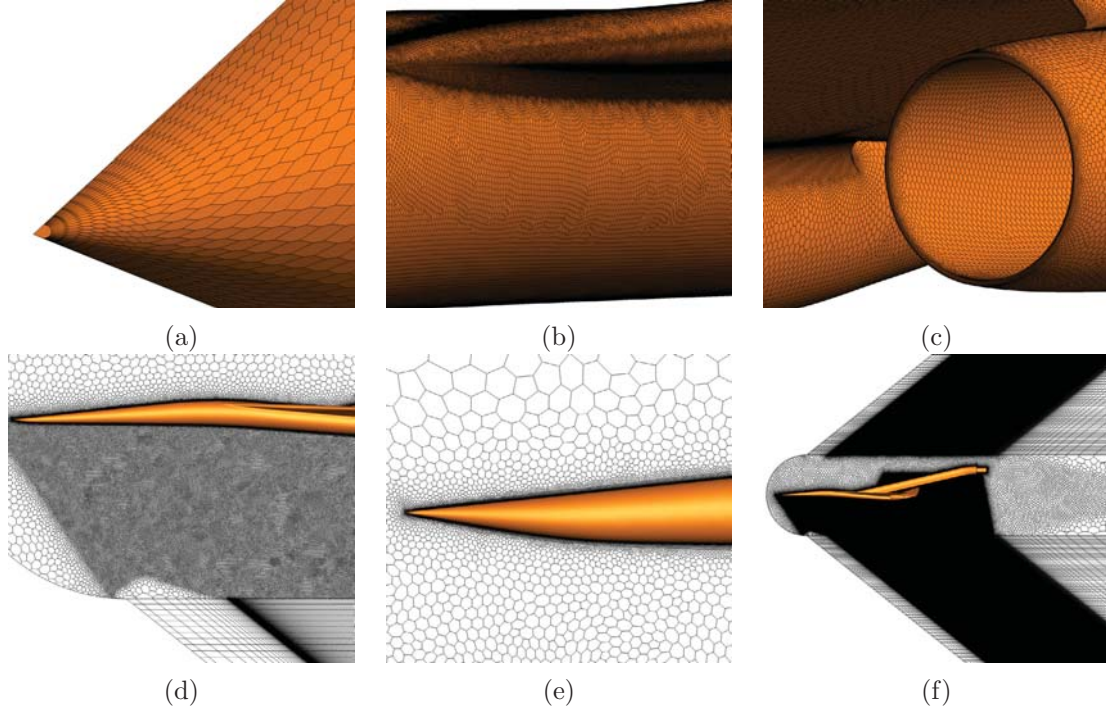(a)　　　　　　　　　(b)　　　　　　　　　(c)

(d)　　　　　　　　　(e)　　　　　　　　　(f)

Figure 17. Images of the structured overlapping grid system for the LM 1012 model. (a-c) Details of the surface grid. (d-f) Details of the Mach-angle aligned off-body grid.

American Institute of Aeronautics and Astronautics

(a)   (b)   (c)

(d)   (e)   (f)

Figure 18. Images of the unstructured polyhedral mesh for the LM 1021 model. (a-c) Details of the surface grid. (d-f) Details of the core mesh and the Mach-angle aligned extrusion.

wake from the blade may effect the inlet conditions to the nacelle, as pointed out by Morgenstern.[28] The simulations were performed at Mach 1.6 with a Reynolds number of 4.36 million and an angle of attack of 2.1 degrees. Experimental data, obtained from Cliff *et. al*,[7] for on-track measurements at this angle of attack are used for validation. Off-track measurements at 2.3 and 2.5 degrees angle of attack are used for comparison purposes.

III.C.1. *Computational Model and Requirements*

The baseline structured overset grid system is comprised of 97 curvilinear structured grids and 72.7 million grid points. The body of the model was meshed with 89 volume grids and 22 million grid points. Figures 17a - c shows three views of the surface grid where each zone is represented by a different color. The configuration was split into several components, and each component was initially meshed independently. Once the grid topologies were complete, the component grids were combined and individual grid spacings are adjusted for proper overset grid communication. Hyperbolic mesh generation was used for these near-body grids with a marching distance of 2 percent of the model reference length. The Mach-angle aligned off-body grid was generated separately for this configuration and utilized 8 zones and 50.7 million grid points. Grid-lines along the axial direction of the Mach-angle aligned mesh were clustered at specific locations for improved overset communication at the leading and trailing edges of the wing and tail, as well as the nacelles. Additional clustering at the nose of the model is used to capture the attached shock. Grid clustering was also utilized in the circumferential direction near the symmetry plane, under-wing nacelle, wing tip, and tail. Details of the Mach-angle aligned grid are illustrated in Figures 17d - f. This strategy for the Mach-angle aligned mesh differs from the approach used to grid the axisymmetric fuselages studied in the previous test cases, and allows the generation for these grids to be separated from the rest of the grid system. This separation can be exploited to allow automated grid generation scripts to be

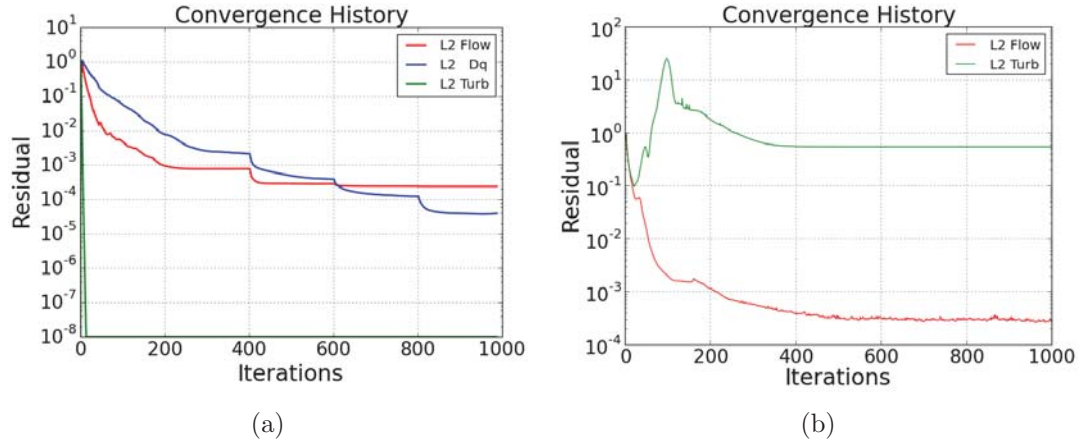American Institute of Aeronautics and Astronautics

Figure 19. Plot of the residual convergence history for the LM 1021 test case using the structured overlapping grid system (a) and the unstructured polyhedral mesh (b).

developed for the Mach-angle aligned grids.

The unstructured mesh was generated using the same strategy employed for the 69° Delta Wing-Body model and utilizes 65.5 million polyhedral cells. First, the surface is tessellated with clustering at the nose, leading and trailing edges of the wing and tail, as well as the inlets and outlets of the nacelles, see Figure 18a - c. Once the surface mesh is complete a polyhedral core grid is generated which encompasses the entire model, a finer spacing specification is used on the symmetry plane surface below the model for improved on-track mesh resolution, as shown in Figure 18d. Once the core grid is complete, prismatic layers are grown from the surface to capture the high gradients in the boundary layer. The prism layers are then transitioned into the core grid, see Figure 18e. The exterior-boundary of the core grid is then stretched in the Mach-angle direction to the outer-boundary of the computational domain, Figure 18f.

As in the previous test cases, converged solutions for the LM 1021 model were obtained in less than 1000 iterations for both the structured and unstructured grids. The overset grid, using the modified Roe numerical flux and the Spalart-Allmaras turbulence model required 1 hour and 30 minutes using 180 ivy bridge cores to complete 1000 iterations. The unstructured grid, using the AUSMPW+ flux and the same turbulence model required 45 minutes on 2000 ivy bridge cores. This equates to 270 core-hours for the structured grid and 1500 core-hours for the unstructured grid. This is a factor of 5.5 times more resources using the unstructured approach. A plot of the residual convergence for both grid approaches is shown in Figure 19. Similar convergence rates are observed for the residual of the continuity equation. The turbulence model converges very rapidly on the structured grid, while on the unstructured grid similar behavior to the DWB test case is found. Reasons for the improved convergence on the structured grid are still under investigation.

III.C.2. Data Comparison

The requested data delivery for the workshop consisted of pressure extracted on five cylindrical surfaces at distances of $h = 19.7$, 31.8, 42.0, 70.0, and 100.7 inches. A schematic of the extraction surfaces (only half of the total azimuth is shown) with pressure contours is plotted in Figure 20. These cylindrical surfaces are mapped to the plane and plotted for both the structured and unstructured results in Figure 21a and b, respectively. Analyzing the two carpet plots, very similar contour levels are observed at each of the five extraction distances on both the structured and unstructured grids. The attached shock generated at the nose, located at the front of the contour section at $h = 19.7$ inches , is captured over all azimuthal angles. As the distance of the model increases, some minor

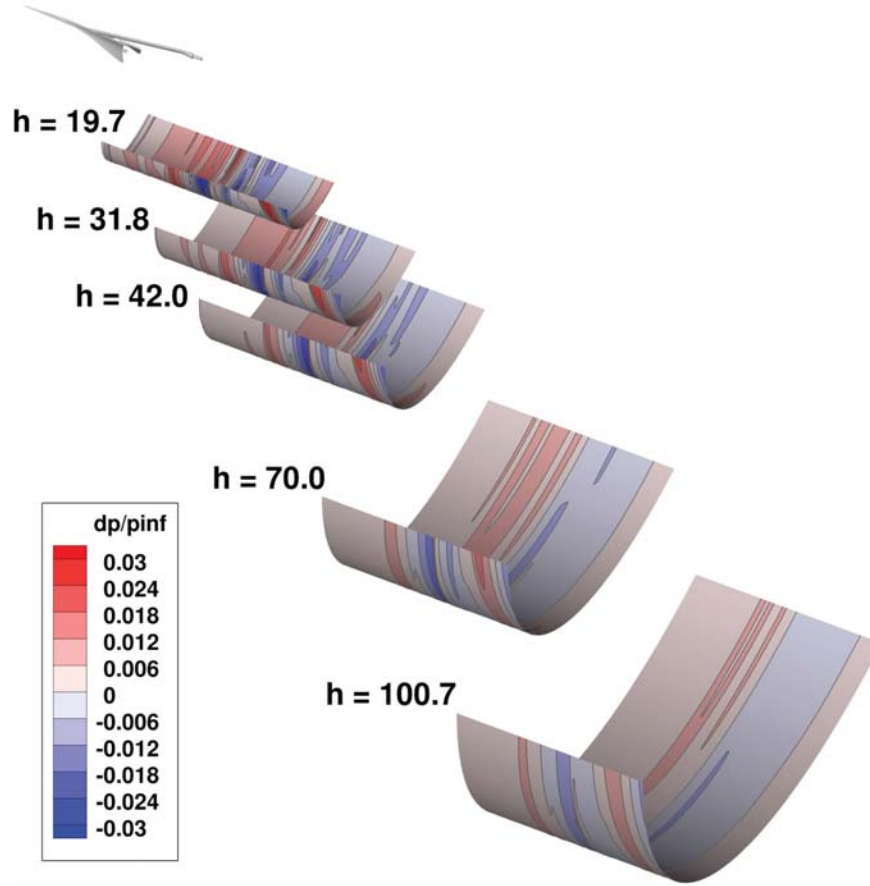American Institute of Aeronautics and Astronautics

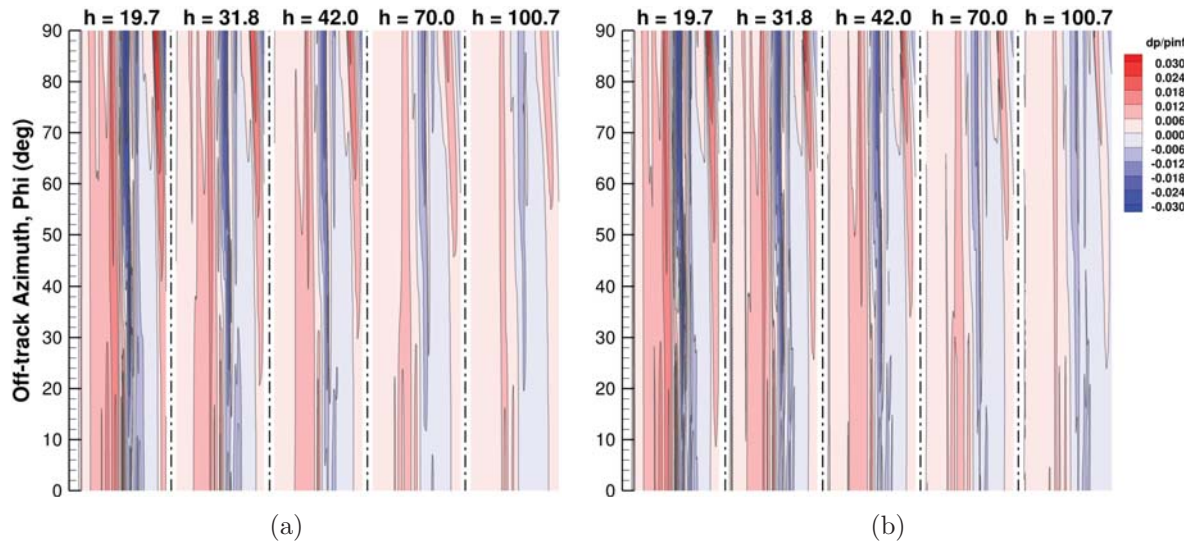Figure 20. Contours of pressure on extractions surfaces for the LM 1021 test case.

Figure 21. Carpet plot of azimuthal pressure variation at five distances from the LM 1021 model h = 19.7, h = 31.8, h = 42.0, h = 70.0, and h = 100.7 inches. Streamwise locations are off-set for visibility. Pressure extracted from the structured (a) and unstructured (b) grid computations.
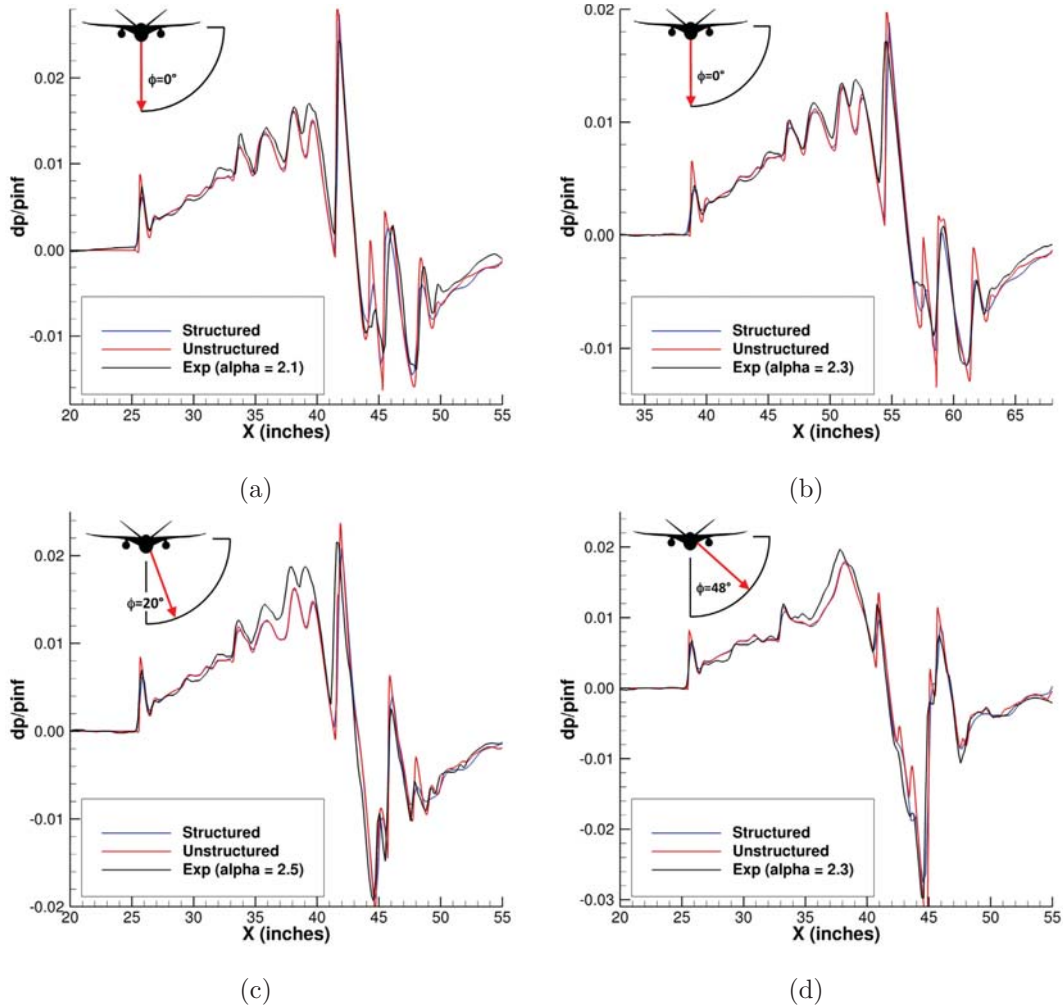
American Institute of Aeronautics and Astronautics

Figure 22. Comparison of CFD predicted pressure signatures versus experimental data for the LM 1021 model at (a) h = 20.8 inches ϕ = 0 degrees, (b) h = 31.3 inches ϕ = 0 degrees, (c) h = 20.8 inches ϕ = 20 degrees, and (d) h = 20.8 inches ϕ = 47 degrees.

distances are observed. For example, towards the end of the contour section at $h = 100.7$ inches, the structured mesh predicts a pressure near 0.007 from $0 \leq \phi \leq 55$ degrees. While on the unstructured grid the 0.007 contour is observed from $24 \leq \phi \leq 67$ degrees. It also appears that the unstructured mesh is capturing some additional pressure perturbations near $\phi = 90$ degrees, which are not found in the structured result.

For a quantitative comparison of the two grid approaches, pressure signatures were extracted at $h = 20.8$ and $\phi = 0$, 20, and 48 degrees, as well as $h = 31.3$, 42.0, and 69.6 inches and $\phi = 0$ degrees. These distances are not identical to the requested data for the workshop, but are at locations where experimental data is available. Figure 22a and b plots the on-track pressure signatures of the CFD predictions against the experimental data at $h = 20.8$ and 31.3 inches. The results from the structured and unstructured grids are almost indistinguishable until $X = 43.5$ inches, then a small off-set is observed. A small over-prediction of the attached shock from the nose is recognized between the CFD and experiment at $h = 20.8$ and $h = 31.3$ inches. The largest overpressure appears to be matched well by the CFD, while the series of shocks emanating from the wing-fuselage intersection
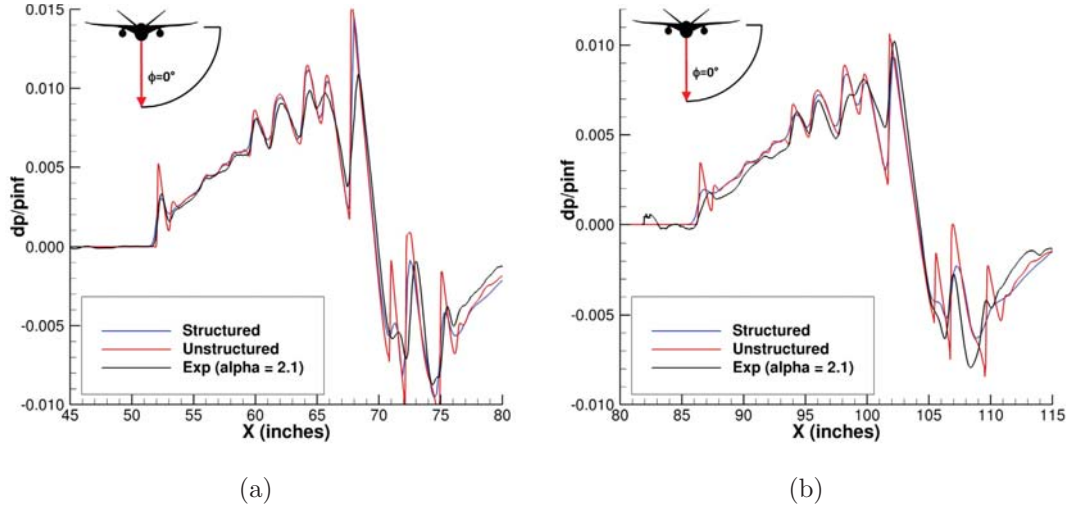
American Institute of Aeronautics and Astronautics

Figure 23. Comparison of on-track CFD predicted pressure signatures versus experimental data for the LM 1021 model at (a) h = 42.0 inches and (b) h = 69.6 inches.

are slightly under-predicted. Examining the off-track signatures in Figure 22c and d, the CFD matches the attached shock strength of the experiment very well, and only a slight over-prediction on the unstructured grid. Downstream of the attached shock, both amplitude and position of the CFD signatures differ from the experiment. This is caused by the difference in the angle of attack recorded in the wind tunnel, which is 2.5 degrees at $\phi = 20$ and 2.3 degrees at $\phi = 48$. The angle of attack in all CFD simulations was 2.1 degrees, as requested in the workshop problem description. In Figure 22d, a flow feature is captured at $X = 43.5$ inches using the structured grid which matches the measured data. A much sharper change in pressure is predicted on the unstructured grid near this location. Further from the model, Figure 23a and b, show a comparison of the on-track pressure signatures at $h = 42.0$ and $h = 69.6$ inches respectively. As before, the structured and unstructured results are very close to each. The comparison to experimental data is relatively good, and all features of the signatures appear to be captured. There is some discrepancy in the magnitude of the larges overpressure at $h = 69.6$ inches, over 3 body lengths away from the model. Overall the comparison is very good, and application of the LAVA solvers to the realistic low boom geometry did not prove to be more difficult than the two mandatory test cases.

III.C.3. *Turbulence Model, Mesh, and Component Sensitivity*

Early wind tunnel tests indicated large laminar flow regions on the LM 1021 model,[28] trip disks were placed along the leading edge of the upper surface of the wing to energize the boundary layer and promote turbulent flow. To assess the sensitivity of the CFD predictions to the fully turbulent flow assumption, a laminar case was performed using the structured grid. Figure 24 shows a comparison of the predicted pressure signatures using fully turbulent and laminar flow assumptions along with experimental data at $h = 20.8$ and $h = 69.6$ inches. Similar to the 69° DWB test case, a constant shift up is observed when using the turbulent flow assumption. The overall discrepancy is only slightly more than what was shown between the structured and unstructured grid approaches. Much larger discrepancies are observed near the surface. Figure 25 plots streamlines on the top and bottom of the model surface for the turbulent and laminar flow assumptions. As indicated by Morgenstern,[28] the blade strut generates a front shock which leads to vortex separation on the upper wing when laminar flow is assumed. This separation is suppressed with the turbulent flow model. In addition, a much larger separation region is generated from the under-wing nacelle for laminar flow, when
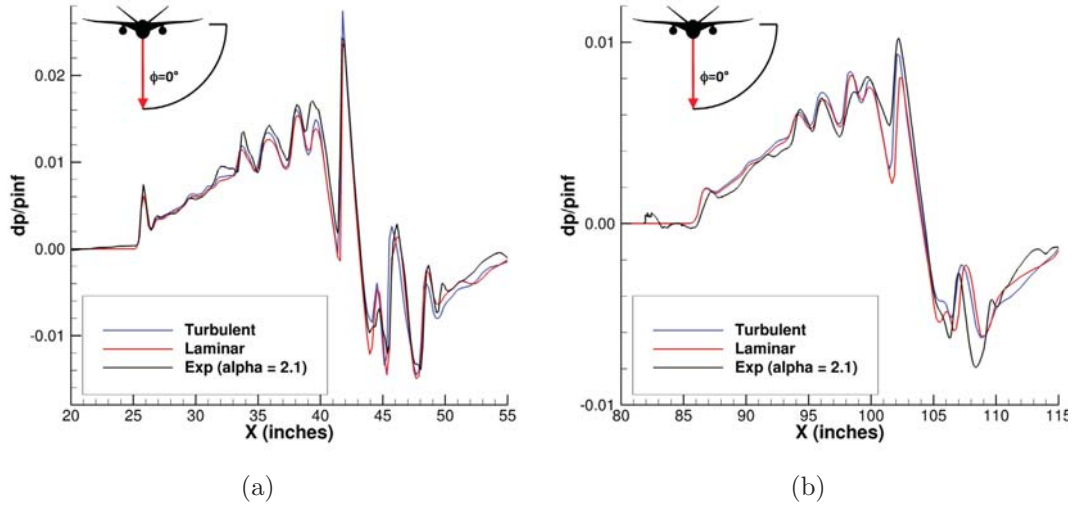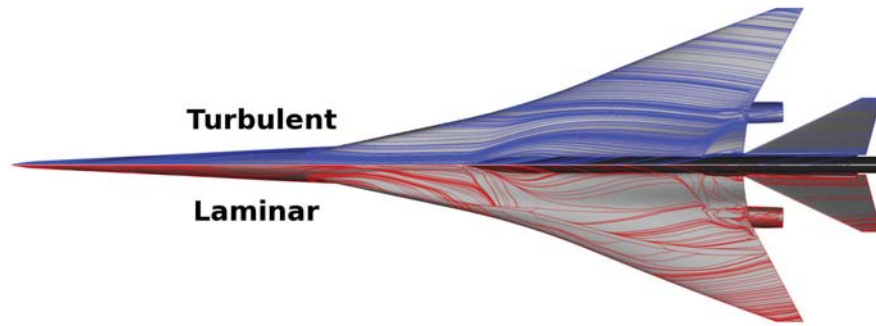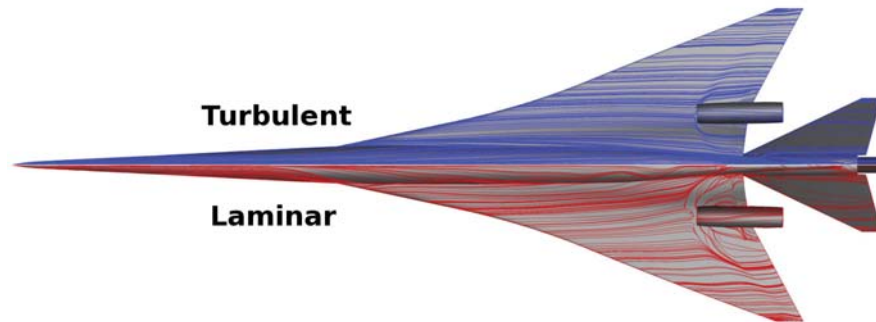
Figure 24. Comparison of CFD predicted on-track pressure signatures using turbulent and laminar flow assumptions versus experimental data for the LM 1021 model at (a) h = 20.8 inches and (b) h = 69.6 inches.

(a) Top

(b) Bottom

Figure 25. Surface streamlines on the (a) top and (b) bottom of the LM 1021 model with the turbulent flow assumption plotted on the top-side of the vehicle in blue and the laminar flow assumption on the bottom-side in red.
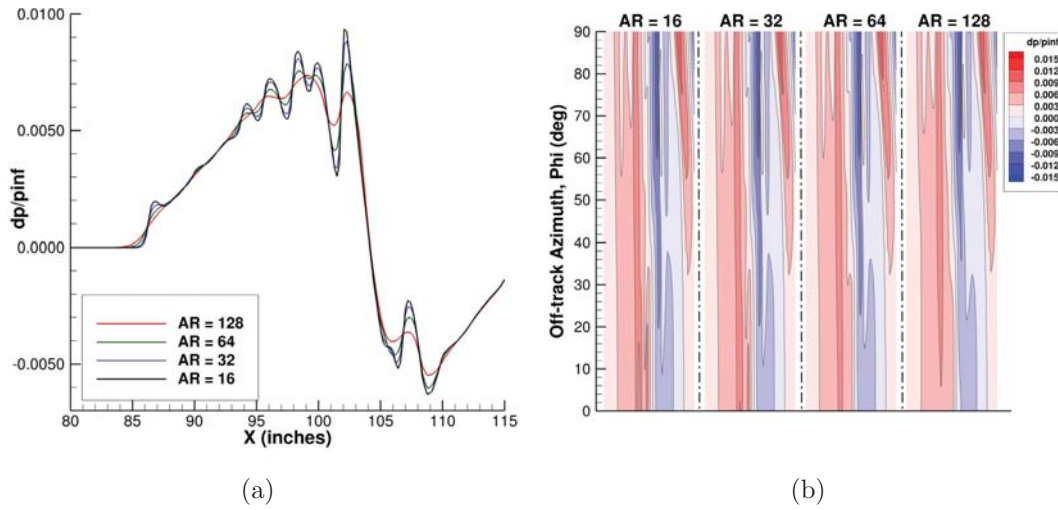
American Institute of Aeronautics and Astronautics

(a)   (b)

Figure 26. (a) Comparison of on-track pressure signature for the LM 1021 model at h = 69.6 inches using four different outer-boundary aspect ratios. (b) Carpet plot of azimuthal pressure variations at h = 70.0 inches for each of the four outer-boundary aspect ratio computations.

compared to turbulent.

The baseline structured overset grid was generated with an outer-boundary aspect ratio of $AR = 16$ based on the aspect ratio study performed on the Seeb-ALR model. Since the number of grid points on the off-body grid is a factor of two times larger than the number of near-body grid points, a sensitivity study on the outer-boundary aspect ratio was also performed for the LM 1021 model. Three-additional overset grid systems were generated with outer-boundary aspect ratios of $AR = 32$, 64, and 128. This reduced the overall grid size to 62.9 million, 56.9 million, and 53.3 million grid points, respectively. Figure 26a plots the pressure signatures at $h = 69.6$ inches from the model and $\phi = 0$ degrees. At an $AR = 128$ the signatures are highly smoothed and many features of the signal are missed. As the aspect ratio is decreased the signals sharpen, and the magnitudes of the peaks appear to be converging at second-order accuracy. To assess the sensitivity of the off-track predictions, a carpet plot of pressure is plotted in Figure 26b. At first glance the pressure contours look very similar, but comparing the $AR = 16$ column with the $AR = 128$ column, many flow features starting at $\phi = 90$ degrees are smoothed out completely by $\phi = 45$ degrees. Since there is no difference in the circumferential resolution between any of these grids, the differences are directly

(a) *No Blade*   (b) *Clean*

Figure 27. (a) Geometry definition for the LM 1021 model with the blade strut remove, designated *No Blade*. (b) Geometry definition of the LM 1021 model with the blade, under-wing nacelle, and pylon removed, designated *Clean*.

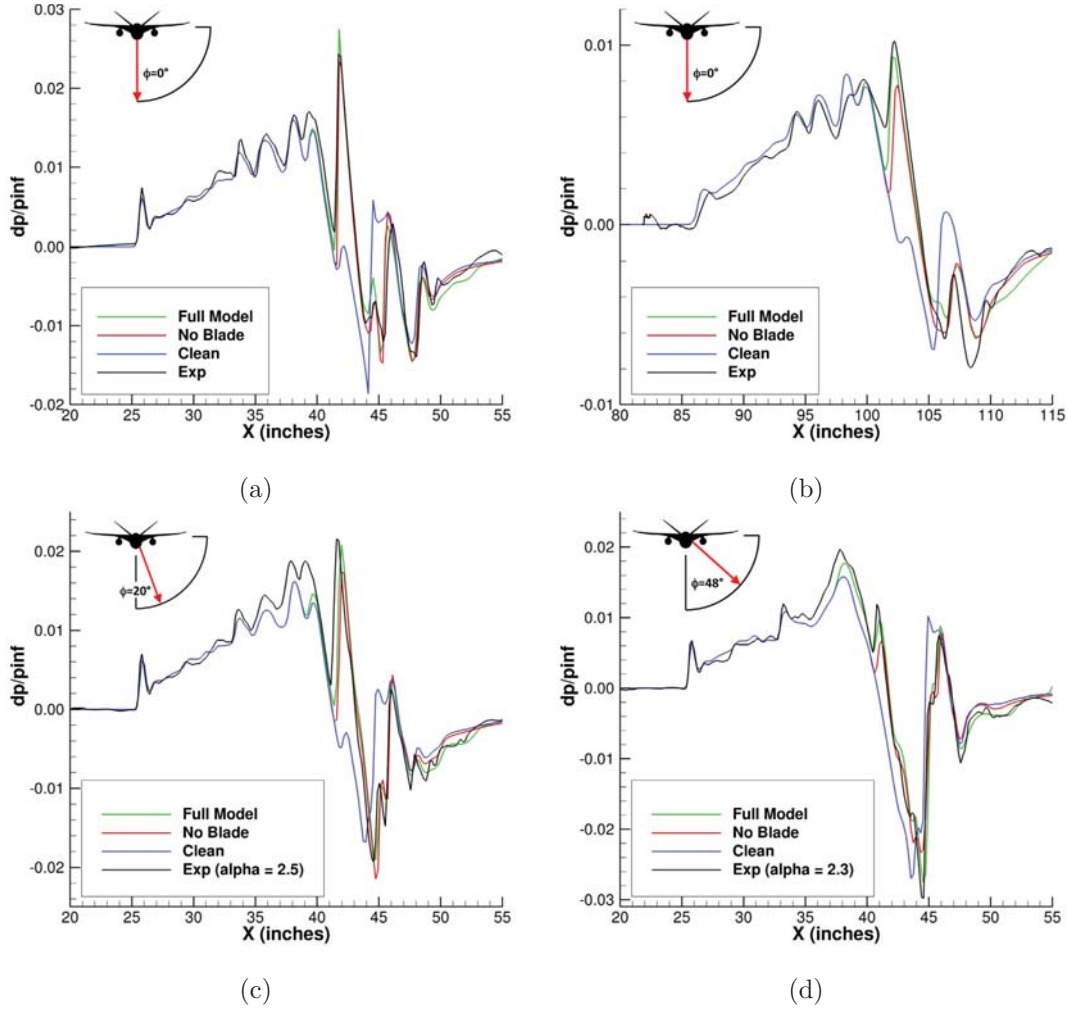American Institute of Aeronautics and Astronautics

(a)

(b)

(c)

(d)

Figure 28. Comparison of the CFD predicted pressure signatures for the full LM 1021 model, the mode with no blade strut, and the model with no strut, under-wing nacelle, or pylon along with experimental data at (a) h = 20.8 inches ϕ = 0 degrees, (b) h = 69.6 inches ϕ = 0 degrees, (c) h = 20.8 inches ϕ = 20 degrees, and (d) h = 20.8 inches ϕ = 47 degrees.

attributed to grid sensitivity to outer-boundary aspect ratio. Since the difference between $AR = 16$ and $AR = 32$ are relatively small, an aspect ratio of $AR = 8$ is not considered in this study.

Influence of the blade support structure on the predicted pressure signature is studied along with an assessment of the contribution of the under-wing nacelle to the sonic boom signature. One advantage of the structured overset grid methodology is the ability to quickly remove components without the need to re-generate the grid system. Using this approach, the blade strut was removed for one configuration (designated *No Blade*) and the under-wing nacelle/pylon along with the strut was removed for a second configuration (designated *Clean*). Perspective images of these two configurations are shown in Figure 27a and b. Pressure signatures were extracted at $h = 20.8$ inches $\phi = 0$, 20, and 48 degrees, and $h = 31.3$ inches $\phi = 0$ degrees for each of the configurations, and plotted in Figure 28. The completed wind tunnel model is designated *Full Model* in these plots. Minor differences on the order of those observed between structured and unstructured approaches are observed between the complete model and the model with no strut. This supports that the

(a) $X = 17.7$ inches

(b) $X = 18.7$ inches

(c) $X = 19.7$ inches
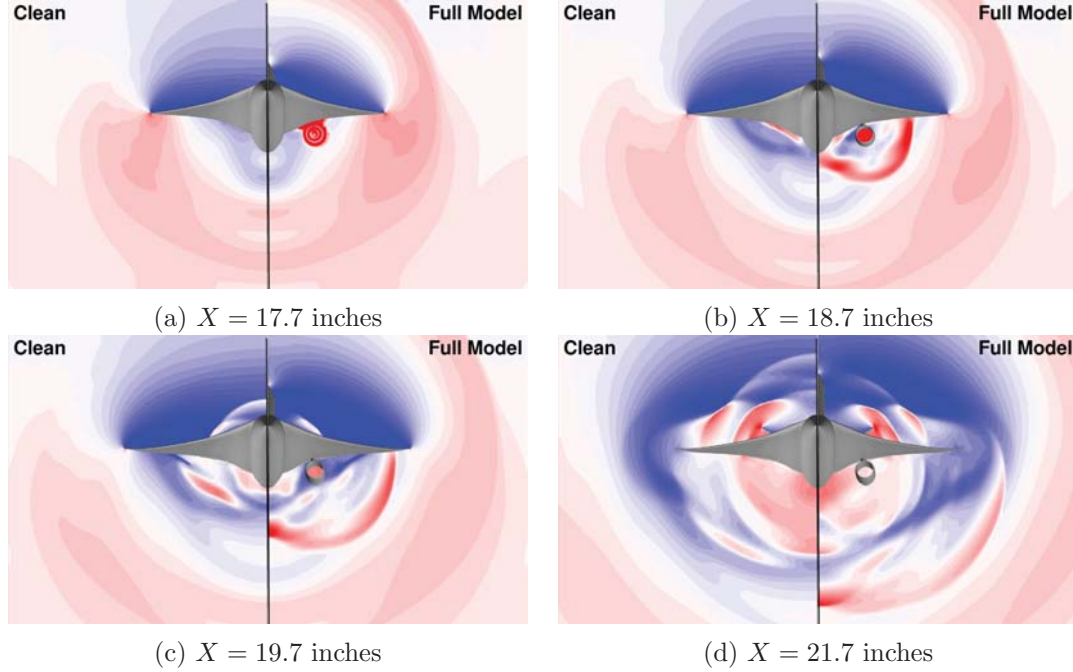
(d) $X = 21.7$ inches

Figure 29. Contour plot of pressure at four streamwise locations (a) X = 17.7, (b) X = 18.7, (c) X = 19.7, and (d) X = 21.7 inches comparing the *Clean* (left) versus the *Full Model* LM 1021 configurations.

strut has minimal effects on the measured pressure signatures in the experiment. More interestingly, removal of the under-wing nacelle dramatically reduces the largest overpressure in the signature at the on-track and 20° degree locations. To explain the large overpressure caused by the under-wing nacelle a sequence of side-by-side contour plots of pressure at four axial locations for both the *Clean* and *Full Model* configurations are shown in Figure 29a - d. A shock is formed at the leading-edge of the nacelle near $X = 17.7$ inches. This shock propagates in the streamwise and radial directions as observed at $X = 18.7$ near the middle of the nacelle, $X = 19.7$ towards the end of the nacelle, and $X = 21.7$ close to the end of the vehicle. This wave represents the large overpressure wave in the pressure signatures which is not generated in the *Clean* configuration. A similar finding was reported by Aftosmis[8] for a different investigation. In their inviscid simulation, a double shock feature was predicted in the large overpressure region. Solution of the adjoint equations were used to trace this difference back to the under-wing nacelle, where a strong viscous shock boundary layer interaction was shown.

IV.   Summary

The Launch Ascent and Vehicle Aerodynamics (LAVA) framework has been successfully applied to the sonic boom prediction workshop test cases. Both structured overset and unstructured grid methodologies have been investigated. The structured overlapping grid systems typically have a larger number of grid points than the corresponding unstructured polyhedral mesh. This is caused by the hyperbolic tangent stretching used for the Mach-angle aligned part of the grid system, rather than the geometric growth used to extrude the unstructured mesh. Similar sonic boom signature accuracy is obtained with both grid methodologies. The total amount of computational resources is between 2 to 5.5 times smaller using structured overset grids when compared to the unstructured polyhedral grid even with a larger number of grid points. In contrast, the unstructured meshes

American Institute of Aeronautics and Astronautics

typically require a factor of 2 to 3 times fewer man hours to generate.

When generating structured overset grids for sonic boom analysis, a general guideline for accurate predictions is to use hyperbolic marching from the body throughout the viscous boundary layer and then transition to a Mach-angle aligned mesh to the outer-boundary. For axisymmetric fuselages, such as the Seeb-ALR and the 69° Delta Wing Body models, the transition between the wall-surface normal and Mach-angle aligned portions can be blended using elliptic smoothing to maintain implicit lines from the body to the outer-boundary. Overset can be used in the transition region for non-axisymmetric fuselages, as was done for the Lockheed-Martin 1021 model, but requires care in properly sizing the mesh at the overset interface region. Solutions are sensitive to the aspect ratio of the cells at the outer-boundary, and sensitivity analysis should be performed. Less sensitivity is observed with respect to circumferential spacing but a maximum of 3 degrees is appropriate.

Good agreement with experimental data was obtained on unstructured grids using the following methodology. First, a cylindrical or elliptic boundary encompassing the vehicle is created and a core isotropic polyhedral mesh is generated. Prism layers are used at the viscous wall boundaries for capturing the sharp gradients in the boundary layer. The boundary of the core grid is then extruded in a Mach-angle aligned direction to the outer-boundary.

Both modified Roe and AUSMPW+ convective flux discretizations performed well on each of the test cases. The predicted pressure signatures using the modified Roe flux appear sharp and monotonic, but slightly more dissipative than the AUSMPW+ results. However, small oscillations are observed across some shocks using AUSMPW+. As expected, central differencing with explicit scalar artificial dissipation creates over- and under shoots at each shock in the signal, but is the least computationally expensive method considered in this analysis.

Acknowledgements

References

[1]Plotkin, K., "Sonic Boom Shaping in Three Dimensions," *29th AIAA Applied Aerodynamics Conference, Honolulu Hawaii*, June 27-30 2011, AIAA-2011-3500.

[2]Aftosmis, M., Nemec, M., and Cliff, S., "Adjoint-Based Low-Boom Design with Cart3D," *29th AIAA Applied Aerodynamics Conference, Honolulu Hawaii*, June 27-30 2011, AIAA-2011-3500.

[3]Morgenstern, J., Norstrud, N., Sokhey, J., Martins, S., and Alonso, J., "Advanced Concept Studies for Supersonic Commercial Transports entering Service in the 2018 to 2020 Period," Technical Report NASA-CR-2013-217820, NASA, 2013.

[4]Waithe, K., "Introduction of First Low Boom Prediction Workshop," *51st AIAA Aerospace Sciences Meeting, Grapevine (Dallas/Ft. Worth), Texas*, January 07-10 2013, AIAA-2013-0650.

[5]Park, M., Campbell, R., Elmiligui, A., Cliff, S., and Nayani, S., "Specialized CFD Grid Generation Methods for Near-Field Sonic Boom Prediction," *52st AIAA Aerospace Sciences Meeting, National Harbor, Maryland*, January 13-17 2014, AIAA-2014-0115.

[6]Saito, Y., Ukai, T., Miyakoshi, K., Ohtani, K., and Obayahsi, S., "Sonic Boom Estimation using the Multipole Method for Free-Flight Experiments," *52st AIAA Aerospace Sciences Meeting, National Harbor, Maryland*, January 13-17 2014, AIAA-2014-0368.

[7]Cliff, A., Durston, D., Elmiligui, A., Jensen, J., and Chan, W., "Computational and Experimental Assessment of Models for the First AIAA Sonic Boom Prediction Workshop," *52st AIAA Aerospace Sciences Meeting, National Harbor, Maryland*, January 13-17 2014, AIAA-2014-0560.

[8]Aftosmis, M. and Nemec, M., "Cart3D Simulations for the First AIAA Sonic Boom Prediction Workshop," *52st AIAA Aerospace Sciences Meeting, National Harbor, Maryland*, January 13-17 2014, AIAA-2014-0558.

[9]Kiris, C., Barad, M., Housman, J., Sozer, E., Brehm, C., and Moini-Yekta, S., "The LAVA Computational Fluid Dynamics Solver," *52st AIAA Aerospace Sciences Meeting, National Harbor, Maryland*, January 13-17 2014, AIAA-2014-0070.

[10]Meredith, K., Dahlin, J., Graham, D. ad Malone, M., Haering, E., Page, J., and Plotkin, K., "Computational Fluid Dynamics Comparisons and Flight Test Measurements of F-5E Off-Body Pressures," *43rd AIAA Aerospace Sciences Meeting, Reno, Nevada*, January 10-13 2005, AIAA-2005-0006.

[11]Haering, E., Murray, J., Purifoy, D., Graham, D., Meredith, K., Ashburn, C., and Stucky, M., "Airborne Shaped Sonic Boom Demonstration Pressure Measurements with Computational Fluid Dynamics Comparisons," *43rd AIAA Aerospace Sciences Meeting, Reno, Nevada*, January 10-13 2005, AIAA-2005-0009.

[12]Cliff, A., Elmiligui, A., Campbell, R., and Thomas, S., "Evaluation of Refined Tetrahedral Meshes with Projected, Stretched, and Sheared Prism Layers for Sonic Boom Analysis," *29th AIAA Applied Aerodynamics Conference*, June 27-30 2011, AIAA-2011-3338.

[13]Cliff, S., Elmiligui, A., Campbell, R., and Thomas, S., "Refined Tetrahedral Meshes with Mach Cone Aligned Prisms for Sonic Boom Analysis," *Journal of Aircraft*, Vol. 50, 2013, pp. 778–790.

[14]Spalart, S. and Allmaras, S., "A One-Equation Turbulence Model for Aerodynamic Flows," *30th Aerospace Sciences Meeting and Exhibit, Reno, NV*, January 1992, AIAA–92–0439.

[15]Menter, F., "Zonal Two Equation k-ω Turbulence Models For Aerodynamic Flows," *23rd Fluid Dynamics, Plasmadynamics, and Lasers Conference, Orlando, FL*, July 1993, AIAA–93–2906.

[16]Spalart, P., Jou, W., Strelets, M., and Allmaras, S., "Comments on the feasibility of LES for wings, and on a hybrid RANS/LES approach," *In Advances in DNS/LES, ed. C Liu, Z Liu, Columbus*, 1997, OH: Greyden Press.

[17]Spalart, P., Deck, S., Shur, M., Squires, K., Strelets, M., and Travin, A., "A new version of detached-eddy simulation, resistant to ambiguous grid densities," *Theo. and Comp. Fluid Dynamics*, Vol. 20(3), 2006, pp. 181–195.

[18]Housman, J., Kiris, C., and Hafez, M., "Time-Derivative Preconditioning Methods for Multicomponent Flows - Part I: Riemann Problems," *Journal of Applied Mechanics*, Vol. 76, No. 2, February 2009.

[19]Housman, J., Kiris, C., and Hafez, M., "Time-Derivative Preconditioning Methods for Multicomponent Flows - Part II: Two-Dimensional Applications," *Journal of Applied Mechanics*, Vol. 76, No. 3, March 2009.

[20]Pulliam, T., "Artificial dissipation models for the Euler equations," *AIAA Journal*, Vol. 24, No. 12, 1986.

[21]Kim, K. H., Kim, C., and Rho, O.-H., "Methods for the Accurate Computations of Hypersonic Flows: I. AUSMPW+ Scheme," *Journal of Computational Physics*, Vol. 174, 2001, pp. 38–80.

[22]George, A. and Seabass, R., "Sonic Boom Minimization Including Both Front and Rear Shocks," *Journal of Aircraft*, Vol. 9, No. 10, 1971, pp. 2091–2093.

[23]Darden, C., "Sonic Boom Minimization with Nose-Bluntness," Technical Report NASA-TP-1348, NASA, 1979.

[24]Chan, W., Gomez, R., Rogers, S., and Buning, P., "Best Practices in Overset Grid Generation," *32nd AIAA Fluid Dynamics Conference and Exhibit, St. Louis, Missouri*, Jun 24-26 2002, AIAA-2002-3191.

[25]Choi, S., Alonso, J., and Ven der Weide, E., "Numerical and Mesh Resolution Requirements for Accurate Sonic Boom Prediction," *Journal of Aircraft*, Vol. 46, No. 4, July-August 2009.

[26]Cliff, S., Elmiligui, A., Aftosmis, M., Thomas, S., Morgenstern, J., and Durston, D., "Design and Evaluation of a Pressure Rail for Sonic Boom Measurements in Wind Tunnels," *Seventh International Conference on Computational Fluid Dynamics, Big Island, Hawaii*, June 2012, ICCFD7-2006.

[27]Hunton, L., Hicks, R., and Mendoza, J., "Some Effects of Wing Planform on Sonic Boom," Technical Note NASA-TN-D-7160, NASA, 1973.

[28]Morgenstern, J., "Full Configuration Low Boom Model and Grids for 2014 Sonic Boom Prediction Workshop," *51st AIAA Aerospace Sciences Meeting, Grapevine (Dallas/Ft. Worth), Texas*, January 07-10 2013, AIAA-2013-0647.